

## Two-dimensional turbulence: a review of some recent experiments

**Hamid Kellay<sup>1</sup> and Walter I Goldburg<sup>2</sup>**

<sup>1</sup> Centre de Physique Moléculaire Optique et Hertzienne, U. Bordeaux I, 351 cours de la Libération, 33405 Talence Cedex, France

<sup>2</sup> Department of Physics and Astronomy, University of Pittsburgh, Pittsburgh, PA 15260, USA

Received 7 February 2001, in final form 9 January 2002

Published 15 April 2002

Online at [stacks.iop.org/RoPP/65/845](http://stacks.iop.org/RoPP/65/845)

### Abstract

A review of recent experiments in two-dimensional turbulence is presented. Work on flowing soap films and on thin layers of fluid driven electromagnetically is covered. Theoretical notions of turbulence in two and three dimensions are introduced.

**Contents**

	Page
1. Introduction	847
2. Theory	848
2.1. Moments	848
2.2. Velocity spectra	851
2.3. Turbulent diffusion	852
3. Early experiments	853
3.1. Decaying grid turbulence in soap films	853
3.2. Forced turbulence in thin layers of fluid on solid substrates	856
4. More recent work	860
4.1. Flowing soap films: decaying and forced turbulence	860
4.2. Two-dimensional mixing studied with a soap film	878
4.3. Work on thin fluid layers on solid substrates	881
4.4. Mixing of a passive scalar	887
5. Relative dispersion	889
6. Conclusion	893
References	893

## 1. Introduction

Until rather recently, two-dimensional (2D) turbulence was the province of the theorist and those who solve the Navier–Stokes equations numerically. To be sure, meteorologists and oceanographers have long found it useful to think of turbulence in the air or in the oceans as being approximately 2D, as far as large-scale eddies are concerned. But it is only in the last decade or so that laboratory studies of quasi-2D turbulence have appeared. The purpose of this review is to present a survey of the more recent work. Our goals are to bring the reader's attention to the fact that 2D turbulence is a subject worthy of interest to the laboratory experimentalist and to promote the development of new techniques for probing this phenomenon.

Like its three-dimensional (3D) antecedent, scaling ideas have proved useful to an understanding of turbulence in two dimensions. But in 2D, dimensional arguments have proved insufficient to explain all observations. Because one cannot avoid the coupling of a quasi-2D system with the solid surfaces or the gaseous phase which surrounds it, one must recognize that large-scale velocity fluctuations will be affected by this coupling. Moreover, the boundaries of the 2D system acquire added importance, because small-scale eddies can, in 2D, combine to form larger eddies, with the upper limit of eddy sizes being set by the system size. Nevertheless, the data suggest there does exist an inertial range in coordinate space and momentum space, where rather universal features of 2D turbulence are to be found.

So far, only two schemes for generating quasi-2D turbulence have emerged. In one of them the turbulence is generated in a relatively thin layer of conducting fluid, with a spatially and temporally varying magnetic field applied perpendicular to this layer. The first such experiment was performed by Sommeria [1]. At about the same time as Sommeria's experiments appeared, Couder demonstrated that vortex interactions and turbulence of the 2D type can also be generated in soap films [2, 3]. With the second technique, the turbulence is generated in a rapidly flowing soap film that is penetrated by a comb (i.e. a one-dimensional grid). The velocity fluctuations appear in the plane of the film, which has a thickness of  $\mu\text{m}$ , whereas the size  $r$  of the eddies produced by the comb range from sub-mm to cm.

Subsequent to the earliest observations of quasi-2D turbulence, many new experimental results have appeared. The above-mentioned two experimental techniques for generating 2D turbulence will be discussed here, as will the measurements themselves. It may be apparent that lowering the dimension  $D$  of the system from three to two will increase the importance of boundary conditions that the experimenter or the theorist imposes on the flow. Boundary effects will therefore be given some attention. The 2D experiments indicate a strong difference between forced and decaying 2D turbulence, an effect that may be, in part, connected with this boundary effect issue.

The paper is organized as follows. The next section contains a brief overview of the theoretical difference between 2D and 3D turbulence; a sharp difference exists because the two-dimensionality of the flow imposes additional boundary conditions on it. In section 3, the two experimental schemes for generating quasi-2D turbulence will be reviewed. The latter type of turbulence can also be created in a flowing stream of electrons placed in an axial magnetic field. This type of electromagnetic turbulence will not be discussed here, in spite of the potentially great importance of this type of experiment [4]. Section 4 is an overview of experimental observations carried out in similar systems. Section 5 presents experimental observations of turbulence in the atmosphere and examines the relevance of 2D turbulence to the dynamics of the atmosphere at large scales.

## 2. Theory

### 2.1. Moments

There is general agreement that all the flow properties of Newtonian fluids in two or three dimensions are encompassed in the Navier–Stokes equation for the velocity  $\mathbf{v}(x, t)$ :

$$D\mathbf{v}/Dt \equiv \partial\mathbf{v}/\partial t + (\mathbf{v} \cdot \nabla)\mathbf{v} = -\nabla p/\rho + \nu \nabla^2 \mathbf{v}, \quad (1)$$

where  $D\mathbf{g}/Dt$  is called the convective derivative of the vector function  $\mathbf{g}$ . Here  $\rho$  is the density of the fluid,  $\nu$  is its kinematic viscosity (viscosity divided by the density) and  $p$  is the pressure. It is assumed here that the fluid is incompressible, i.e.  $\nabla \cdot \mathbf{v} = 0$ . The difference between 2D and 3D flows is not apparent from this equation but becomes so on taking its curl to obtain an equation for the vorticity  $\boldsymbol{\omega} = \nabla \times \mathbf{v}$  of an incompressible fluid. For each component,  $i$ , of  $\boldsymbol{\omega}$  and  $\mathbf{v}$

$$D\omega_i/Dt \equiv (\boldsymbol{\omega} \cdot \nabla)v_i + \nu \nabla^2 \omega_i. \quad (2)$$

Consider the special case where, at a certain instant of time,  $\boldsymbol{\omega} = (0, 0, \omega_z)$ , with the viscous damping term being small. Then  $D\omega_z/Dt = \omega_z \partial u_z / \partial z$ . If  $\partial u_z / \partial z > 0$ ,  $\omega_z$  will momentarily commence growing at an exponential rate. Clearly the vorticity is not a conserved quantity in 3D; it can be magnified by appropriately oriented velocity gradients. As an example, imagine water circulating as it flows downward through a funnel. By conservation of angular momentum, the flow will pick up angular speed as it proceeds downward through the contraction, so that the magnitude of the vorticity is increased in the direction of the velocity gradient. This amplification effect is called *vortex stretching*.

Vortex stretching is absent in two dimensions, because the velocity gradient is always perpendicular to the vorticity, which is necessarily perpendicular to the plane of motion. Hence the first term on the right in equation (2) is absent, assuring that for an inviscid fluid

$$D\omega/Dt = 0$$

if forcing is absent. Of course,  $\boldsymbol{\omega}(\mathbf{r}, t)$  can change locally, but its mean value averaged over the sample area  $A$

$$Z = (1/A) \int \omega^2 d^2 r \quad (3)$$

is a constant of the motion, as are all other vorticity moments. This quantity is called the enstrophy.

In this same inviscid limit, the kinetic energy of the fluid per unit mass  $\mathcal{E}$  in any number of dimensions is conserved:

$$\mathcal{E} = (1/A) \frac{1}{2} \int \mathbf{v}^2 d^2 r. \quad (4)$$

In a real fluid, where the kinetic energy of the flow is ultimately converted into heat through the viscosity term in equation (1), one must continuously inject energy (and enstrophy for a 2D system) if the turbulent fluid is to be kept in a steady state. The energy and enstrophy injection rates  $\epsilon$  and  $\beta$  are, respectively,

$$\epsilon = -d\mathcal{E}/dt \quad (5)$$

and

$$\beta = dZ/dt, \quad (6)$$

the latter being of interest only in two dimensions. The strength of the nonlinear term in equation (1) in 2D and 3D turbulence is governed by the ratio of the convective derivative

term to the dissipative term. From dimensional considerations, this ratio, called the Reynolds number  $Re$ , has the form

$$Re = UL/v, \quad (7)$$

where  $U$  and  $L$  are characteristic velocities and lengths in the turbulent system, respectively. For example,  $U$  might be taken to be the mean flow speed or the rms velocity fluctuations  $v_{\text{rms}}$  of the turbulent flow, and  $L$  might be an aperture size of a grid in 2D or 3D turbulence. Quite often  $L$  is taken to be the ‘Taylor microscale’  $\lambda$ , which is often defined as

$$\lambda = v_{\text{rms}} / \sqrt{\langle (\partial v_x / \partial x)^2 \rangle},$$

with  $x$  taken as the direction of the mean flow. A flow is said to be appreciably turbulent when the Reynolds number  $Re_\lambda$  is more than 100. The brackets denote a statistical average or, where appropriate, a time average.

It is useful to divide 2D and 3D turbulence into two types: *forced* steady-state turbulence, such as that which is produced in a closed vessel containing a stirring device of some sort, and *decaying* turbulence. The latter can also be generated in a closed container, after the stirring device has been shut off. Decaying turbulence is also generated in open systems, such as a water tunnel or wind tunnel with a grid located at the upstream end. The grid generates turbulence on a scale of the mesh size. It decays downstream, being swept there by the mean flow. In writing down equation (1) no forcing term has been included, so this equation pertains to decaying turbulence. It turns out that the distinction between these two types of turbulence is more important in 2D flows than in 3D.

Most studies of 3D turbulence are concerned with velocity fluctuations appearing at scales  $r$  smaller than the scale at which the velocity fluctuations are generated. This is because one is interested in universal features of the velocity fluctuations at small enough scales that they are not influenced by the boundaries. If the turbulence is generated by a grid, of mesh size  $r_{\text{inj}}$ , which will be called the injection scale, there will also be fluctuations on even larger scales, the maximum scale being, say, the smallest lateral dimensions  $L_0$  of the tunnel. In 3D turbulence there is less interest in the mean square velocity fluctuations  $\langle \delta v(r)^2 \rangle$  on scales  $r_{\text{inj}} < r < L_0$ , but even there some universal features of the turbulence are seen [14]. In 2D, on the other hand, velocity fluctuations in this range are extremely important, as we will see, because they carry most of the turbulent kinetic energy.

For 3D flows, one can invoke a dimensional argument that gives the  $r$  dependence of the mean square magnitude  $\langle (\delta v(r))^2 \rangle$ . Assume that the large eddies break up into increasingly smaller eddies  $r_0 \rightarrow r_0/2 \rightarrow r_0/2^2 \dots r_0/2^m \dots$ . Suppose further that this cascade to ever smaller eddies takes place through a wide range of scales,  $r_n = r_0/2^n$ , without conversion of the turbulent kinetic energy into heat. Only at some very small scale  $r \simeq r_d$  are velocity gradients large enough to give significant weight to the Laplacian term proportional to  $v$  in equation (1). The interesting turbulent scales lie in the inertial range of eddy sizes,  $r_0 \gg r \gg r_d$ , where  $r_d$  is a scale so small that the viscous damping term in equation (1) becomes as large as the inertial term  $(v \cdot \nabla)v$ . One way to define  $r_d$  is to introduce an  $r$ -dependent Reynolds number  $Re(r) = \delta v(r)r/v$ , with the dissipative scale defined by  $Re(r_d) = 1$ . Here, as with other definitions of  $r_d$ , decreasing  $v$ , at a fixed energy injection rate, extends the inertial range to smaller scales.

There are very few exact results pertaining to turbulent flows. The most notable one derived by Kolmogorov [5–7] pertains to the longitudinal third moment of velocity differences on scales  $r$ , where the longitudinal  $n$ th moment is defined as

$$S_n = \langle (v(x+r) - v(x)) \cdot r / r^n \rangle \equiv \langle \delta v(r)^n \rangle. \quad (8)$$

Kolmogorov showed that for decaying 3D homogeneous, isotropic turbulence,

$$S_3(r) = -4/5\epsilon r \quad (9)$$

plus a term proportional to  $v$  and which will not be written down just yet. Additionally, there is a term containing the time derivative of a (decaying) velocity autocorrelation function. It is small in 3D [7], but not in 2D, and we will come back to it.

Because the flow is assumed to be homogeneous, the largest eddy size  $L_0$  is implicitly assumed to be infinite. For decaying turbulence, there is actually a third term in  $S_3$  that involves the time derivative of a velocity–velocity correlation function, but this term is expected to be small [7], at least for 3D flows. In the forced steady state this term is absent, but the above expression for  $S_3$  nevertheless remains valid [5]. We will see that this velocity correlation term appears to play an important role in 2D decaying turbulence.

There is no way to calculate rigorously any moment of velocity differences other than  $S_3$ , but we can, following the lead of Richardson [8] and Kolmogorov [6], estimate the  $r$  dependence of all moments in the inertial range in 3D. The starting point is the definition of  $\epsilon$  given in equation (5). Assume that the energy, injected at some large scale  $r_{\text{inj}}$ , cascades down to smaller scales, the smallest one of interest here being  $r_d$ . In the inertial range, by its definition, the magnitude of velocity fluctuations  $\delta v(r)$  does not depend on  $v$  but will, of necessity, depend on  $\epsilon$ .

If the injected energy flux is not dissipated into heat at any step of the cascade,  $\epsilon$  should be of the order of  $\delta v(r)^2/\tau_r$ , where  $\tau_r$  is the lifetime of an eddy of size  $r$ . In order of magnitude, it is reasonable to replace  $\tau_r$  by  $r/\delta v(r)$ , where  $\delta v(r)$  is the characteristic amplitude of a velocity on the scale  $r$ . Thus,  $\epsilon \simeq \delta v(r)^3/r$  or, equivalently,

$$\delta v(r) \simeq (\epsilon r)^{1/3}. \quad (10)$$

Because  $\delta v(r)$  is a random variable, the left side of this equation is more accurately identified with  $\sqrt{\langle \delta v(r)^2 \rangle}$ .

The small-scale end of the inertial range can alternatively be defined by the relation  $\tau_{r_d} (= r_d/\delta v(r_d)) = r_d^2/v$ , with the term on the right being of the order of the viscous damping time of an eddy of this size. Taking  $\delta v(r_d) = (\epsilon r_d)^{1/3}$ , one obtains from these equations the result

$$r_d = [v^3/\epsilon]^{1/4}. \quad (11)$$

In the dissipative range  $r \leq r_d$ , where  $Re(r_d) = 1$ , the inertial-range cascade is no longer present, and the velocity field now consists of small regions of local shear that are random in both magnitude and direction. In this small- $r$  range, mean square differences  $S_2(r) = \langle \delta v(r)^2 \rangle$  will be proportional to  $r^2$ , and likewise the *absolute moments*  $G(r) = \langle |\delta v(r)|^n \rangle$  should scale as  $r^n$ , according to the above dimensional argument.

Kolmogorov's 3D third moment derivation might lead one to expect that all longitudinal moments will scale as  $S_n(r) \propto r^{\zeta_n}$  with  $\zeta(n) = n/3$  in the inertial range. For small  $n$  this prediction is in agreement with experiment [5] but, as  $n$  increases,  $\zeta_n/n$  decreases with increasing  $n$ . Much of modern day turbulence research centres on efforts to understand the functional form of  $\zeta(n)$  [5].

One can repeat the Kolmogorov derivation for decaying 2D turbulence. The calculation shows that only the coefficient '4/5' in equation (9) is changed, and one now gets  $S_3(r) = -(3/2)\epsilon r$ . Measurements of this third moment, to be discussed below, show that the interval in which  $S_3$  is proportional to  $r$  is very small.

In the inertial range of 2D turbulence, where  $Z$  is conserved as well as  $\mathcal{E}$ , a dimensional argument, like that given above, suggests the existence of a range of scales where

$$S_2(r) \propto \beta^{2/3} r^2, \quad (12)$$

since  $\beta$  has the dimensions of  $s^{-3}$ . This argument considers that the enstrophy injection rate  $\beta$  and the scale  $r$  are the only relevant physical parameters in this range. In this so-called enstrophy range,  $S_2$  is seen to vary with the same power of  $r$  as in the dissipative range, blurring the determination of the boundary between the two. The smallest length scale in the enstrophy range is  $r_d$ , which must depend on both  $\beta$  and  $\nu$ , and a dimensional argument like that invoked to yield the dissipative scale in 3D yields  $r_d \simeq \nu^{1/2} \beta^{-1/6}$ .

The difference between 2D and 3D turbulence is illuminated by considering how the mean square vorticity varies as  $\nu$  is decreased. For isotropic turbulence, the energy injection rate and enstrophy  $Z$  are related by [5]

$$\epsilon = \frac{1}{2} \nu \langle \omega^2 \rangle = \frac{1}{2} \nu Z \quad (13)$$

where  $Z$  is a constant of the motion and cannot diverge in 2D. Thus, decreasing  $\nu$  will drive  $\epsilon$  to zero rather than generating a divergence in  $Z$ ; in 3D,  $Z$  can be amplified by vortex stretching. This decrease in  $\epsilon$  with decreasing  $\nu$  is accomplished by the organization of eddies into structures larger than the injection size  $r_{\text{inj}}$ . The injection scale might be the tooth spacing of the comb in the soap film experiments or the spacing of magnets in those involving a thin layer of conducting fluid.

Summarizing the above dimensional arguments for 2D turbulence:

$$\begin{aligned} S_2(r) &\sim (\epsilon r)^{2/3} & L_0 &> r > r_{\text{inj}} \\ S_2(r) &\sim \beta^{2/3} r^2 & r_{\text{inj}} &> r > r_d \\ S_2(r) &\sim (\beta/\nu) r^2 & r &< r_d = \nu^{1/2} \beta^{-1/6}. \end{aligned} \quad (14)$$

As before,  $L_0$  is the characteristic size of the 2D system.

These equations would remain dimensionally correct if the right sides were multiplied by a correction factor of the form  $\log r/r_{\text{inj}}$  (with the unknown parameter  $r_{\text{inj}} < r$  to keep  $S_2$  positive). Indeed one expects such a correction in the enstrophy cascade range [12]. Admittedly, this logarithmic factor could be difficult to measure in the face of the quadratic variation of  $S_2$  with  $r$  in equation (14). In contrast, the logarithmic term is expected to be the only one present in the 2D vorticity structure function, which we consider next.

The logarithmic correction factor in the above equations should be more easily observable in a measurement of the vorticity structure function  $W_2$ , defined in analogy with  $S_2(r)$ , i.e.  $W_2(r) = \langle (\omega(\mathbf{x} + \mathbf{r}) - \omega(\mathbf{x}))^2 \rangle = 2Z - 2C_\omega(r)$  where  $C_\omega(r) = \langle \omega(\mathbf{x})\omega(\mathbf{x} + \mathbf{r}) \rangle$ . In the enstrophy cascade range,  $W_2$  should depend only on  $\beta$ , so that  $W_2(r)$ , which has dimensions of  $s^{-2}$ , cannot depend on  $r$ , logarithmic corrections aside. Thus  $W_2(r)$  should not approach zero as  $r \rightarrow 0$ . Dimensional arguments are best applied to the cross-term  $C_\omega(r)$ . Indeed one expects it to scale as a power of  $\log(r/r_{\text{inj}})$ . Falkovich and Lebedev [13] have argued that, in steady-state 2D turbulence in the enstrophy cascade range,  $C_\omega(r) \propto [\beta \log(r_{\text{inj}}/r)]^{2/3}$ . We are unaware of any laboratory measurements of this correlation function.

The inverse 2D cascade is a dramatic new effect, revealed in the experiments to be discussed in the next section. Those measurements are in wavenumber space as well as coordinate space.

## 2.2. Velocity spectra

Decomposing the velocity field in  $d$  dimensions into its spatial Fourier components, one has

$$\mathbf{v}(\mathbf{k}, t) = (1/2\pi)^d \int_{-\infty}^{\infty} \mathbf{v}(\mathbf{r}, t) e^{-i\mathbf{k}\cdot\mathbf{r}} d\mathbf{r}. \quad (15)$$

The nonlinear term in the Navier–Stokes equation couples velocity fluctuations of wavenumber  $\mathbf{k}$ . Of special interest is the energy density per unit wavenumber per unit mass,  $E(k)$ , for

homogeneous and isotropic turbulence. This quantity is defined so that

$$\mathcal{E} = \frac{1}{2} \langle \mathbf{v}^2 \rangle = \int_0^\infty E(k) dk \quad (16)$$

where  $k = \sqrt{k^2}$  is the magnitude of a vector in two or three dimensions. In all dimensions,  $E(k)$  has units of  $\text{m}^3 \text{s}^{-2}$ . Invoking the Wiener–Khintchine theorem [5], one can show that  $E(k)$  is proportional to the Fourier transform of  $\langle \mathbf{v}(\mathbf{x}) \cdot \mathbf{v}(\mathbf{x} + \mathbf{r}) \rangle$ , where both velocity components are measured at the same time  $t$  [5].

From dimensional arguments or the cascade picture it follows that, in 2D or 3D,

$$E(k) = \text{const } \epsilon^{2/3} k^{-5/3} \quad k_d < k < k_{\text{inj}}, \quad (17)$$

where  $k_d = 1/r_d$  (sometimes  $k_d$  is defined as  $\pi/r_d$  or  $2\pi/r_d$ ).

In 3D experiments, there is much evidence to support this ‘five-thirds law’ in the inertial range [5]. In most experiments,  $E(k)$  is extracted from a measurement of the longitudinal velocity correlation function  $C(r) = \langle v_x(\mathbf{x}, t) v_x(\mathbf{x} + \mathbf{r}, t) \rangle$ , where  $y$  and  $z$  are fixed, and with  $\mathbf{x}$  and  $\mathbf{x} + \mathbf{r}$  being two co-linear points in the direction of the mean flow. In 2D, where only a few spectral measurements have been made, the Wiener–Kinchine theorem, applied to isotropic turbulence, gives

$$E(k) = A \int_0^\infty [C(x) \cos kx] dx, \quad (18)$$

where  $A = 1/\pi$  to ensure that  $\int_0^\infty E(k) dk = \langle \mathbf{v}^2 \rangle$ .

In the enstrophy range, dimensional considerations dictate that, in 2D,

$$E(k) = \text{const } \beta^{2/3} k^{-3} \quad k_{\text{inj}} < k < k_d \quad (19)$$

if  $E(k)$  is to vary as a power of  $k$ . In the dissipative range,  $k > k_d = (\beta/v^3)^{1/6}$ .

$E(k)$  appears to fall off more rapidly than any power of  $k$  [14]. The same is true of 3D spectra. In momentum space, as in coordinate space, one expects a logarithmic correction to  $E(k)$  and to the enstrophy correlation function  $\hat{C}_\omega(k)$ , the Fourier transform of the vorticity correlation  $C_\omega(r)$ . Kraichnan has argued that  $\hat{C}_\omega(k) \simeq \beta^{2/3} (\log(k/k_0))^{2/3}$  [12]. Again, this logarithmic behaviour has not yet been observed in the laboratory.

### 2.3. Turbulent diffusion

Consider next a measurement of the separation  $r(t)$  of a pair of tagged fluid particles or other test particles, such a pair of balloons, or smoke particles moving in a turbulent fluid. In this case the *turbulent diffusivity*  $D(r)$ , will depend on the separation  $r(t)$ ; particles that are initially very close together will follow almost identical paths, at least for a short time interval, so that  $D(r)$  will be zero. On the other hand, when  $r(t)$  becomes large, the particles will move in widely separated eddies, and  $D(r)$  will be correspondingly large. Dimensional arguments again yield an estimate of the turbulent diffusivity (also called the Richardson 4/3 law) [14]:

$$D(r) = d\langle r^2 \rangle / dt \sim 2r d\langle r \rangle / dt = r |\delta v(r)| \propto r (\epsilon r)^{1/3} \simeq r^{4/3}. \quad (20)$$

For turbulent fluctuations on sufficiently large scales that the motion of fluid elements is completely uncorrelated,  $D(r)$  will become independent of  $r$ , as in Brownian motion.

Integration of the above equation yields the time dependence of the mean square particle separation  $\langle r(t)^2 \rangle$ , a quantity that might be measured by photographing a cloud of particles of initial size  $r_i(0)$ . The turbulence will expand the cloud, giving it a mean radius  $r(t) \gg r_i(0)$

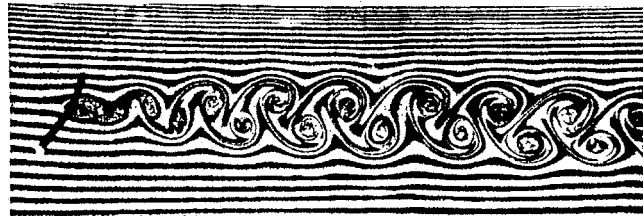


**Figure 1.** von Karman street generated by towing a small cylinder through a still horizontal soap film.

after a long interval of time. An ensemble of such measurements yields  $\langle r(t)^2 \rangle$ . If  $r_i$  is in the inverse cascade range

$$\langle r(t)^2 \rangle \propto t^3.$$

If the initial cloud size is so small as to be in the enstrophy range, and if  $r(t)$  is also in this range, the same sort of dimensional argument now gives

$$\langle r(t)^2 \rangle \propto e^{p\beta^{1/3}t}$$

with  $p$  a dimensionless constant [16].

### 3. Early experiments

Only two different schemes have emerged in the past couple of decades to probe 2D turbulence and hydrodynamics in the laboratory. This first section covers the two pioneering experiments carried out in the 1980s and which show quasi-2D hydrodynamic behaviour. One of these experiments was carried out by Couder [3] and collaborators using soap films; the other by Sommeria [1], who made measurements on thin layers of mercury on a solid substrate where the forcing was supplied by electric currents and a static vertical magnetic field. The first experiment focused on the decay of the turbulence created by a grid towed through the film. In the second type of experiment, the turbulence is forced into a steady state, enabling observation of an inverse cascade of energy. These experiments are summarized in the following subsections.

#### 3.1. Decaying grid turbulence in soap films

This is one of the first experiments where a soap film is used to study turbulent quasi-2D hydrodynamics [3]. These thin liquid soap films can be prepared with a thickness of a few micrometres and a lateral extent of several square centimetres, giving very large aspect ratios. The velocity field in the film can be considered as 2D, since its fluctuations perpendicular to the film plane are heavily damped by viscosity. Ignoring these very small fluctuations, the vorticity is perpendicular to this plane, as required of 2D turbulence. Thus the vortex stretching effect, characteristic of 3D flows, is suppressed in these very thin films.

Couder towed a cylinder through a soap film and could photograph the von Karman street it generated (see figure 1). The images are taken in reflection using monochromatic light (from a sodium lamp); regions of different thickness reflect light differently, leading to the interference patterns seen. Soap films thus provide a natural way to visualize the 2D flow.

A few studies have been devoted to the interpretation of the thickness variations due to hydrodynamic flows in soap films [20, 21, 23]. The issue of the coupling between thickness and

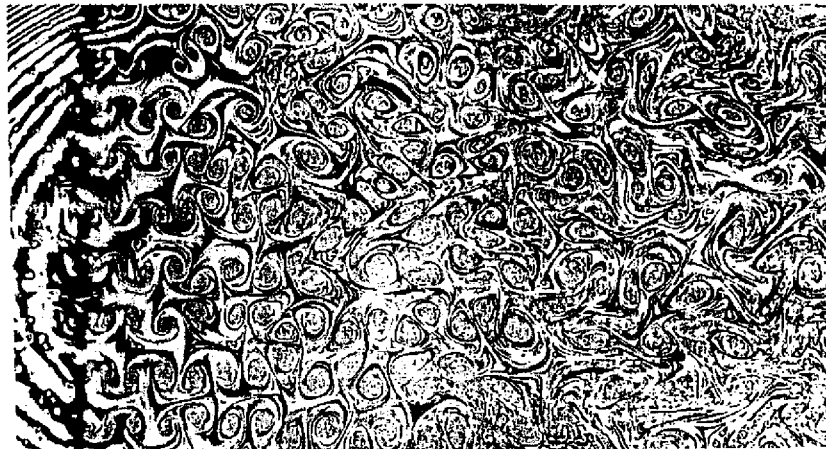


**Figure 2.** Grid generated turbulence obtained by towing an array of cylinders through a still horizontal soap film.

velocity fields remains open, however. A soap film is a thin layer of water bounded by a pair of surfactant monolayers. If the soap concentration exceeds the critical micelle concentration, the interior of the film will also contain spherical or cylindrical micelle structures. The composition of soap films is typically 98 or 99% water, with the remaining component being commercial detergent or a pure surfactant. For more information on the properties of soap films we refer the reader to the book by Mysels *et al* [24].

These soap films are thick when they form but drain with time to very small thickness. In this experiment the soap films are obtained by dipping a frame, of typical size 0.1 m on a side, in the soap solution. The film forms around the edges of the frame. The draining time for a film of initial thickness  $h$ , of the order of tens of  $\mu\text{m}$  down to a few  $\mu\text{m}$ , is tens of seconds.

The film takes on a relatively constant thickness in the middle of the frame. The experiments are carried out while the film keeps a relatively constant thickness and before it thins down to a thickness that can be as small as 10 nm at the end of the draining process. Regions of the film having this thickness, of course, reflect no light. Glycerol added to the soap solution slows down the draining and was used in this experiment to reduce the effect of the reduction of thickness of the film during the measurements.

In order to produce an initially turbulent flow, Couder towed a grid formed from an array of cylinders 0.2 cm in diameter with a spacing of 0.1 or 0.2 cm between the cylinders. The towing speed was constant and typically  $60 \text{ cm s}^{-1}$ . An estimate of the Reynolds number, based on the size of the cylinders and assuming a film kinematic viscosity similar to that for water, gives a value of about 1200. However, the kinematic viscosity of soap films can differ considerably from that of water and values close to ten times this value have been reported before. The wakes from each cylinder interact strongly after they are formed, giving way to a turbulent flow field like that shown in figure 2. The measurements focus on the size of the vortices and their evolution in time after the passage of the grid.

The main observation is that the passage of the array of cylinders or grid generates several vortices which then interact strongly, generating pairs of (equal-chirality) vortices which eventually merge to form larger ones. This vortex merging is believed to be the main mechanism for the increase of the typical scales of a turbulent 2D flow. The typical size of the vortices was observed to increase as time elapses after the passage of the grid. No more

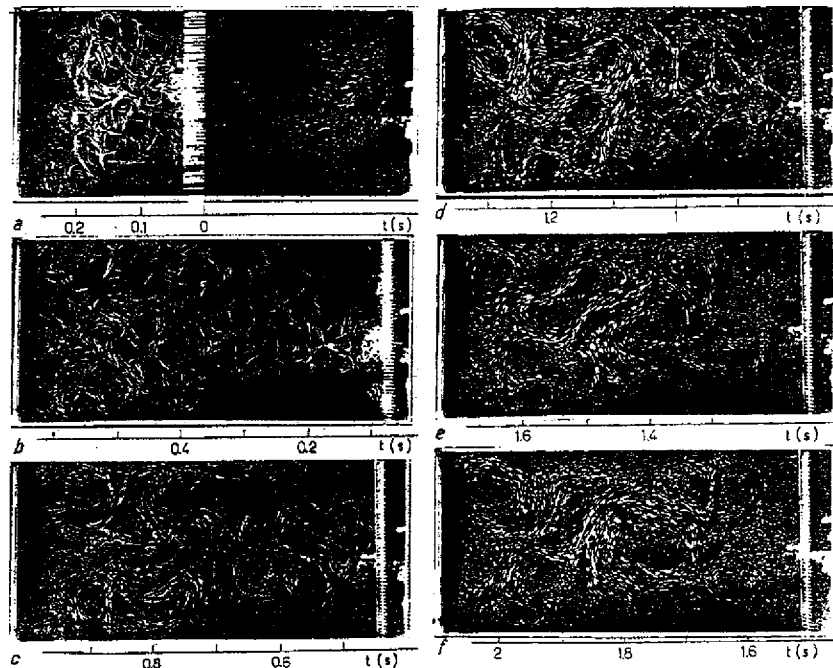


**Figure 3.** The figure shows six photographs taken 0.36 s apart showing the flow. The size of the frame ( $1.58 \times 33$  cm) gives the scale.

kinetic energy is injected into the flow and the initial turbulence generated by the passage of the grid must decay in time.

Bachelor predicts that, during this decay of the turbulence, the characteristic scale of the flow increases with time in a linear fashion. In the experiments of Couder, the typical vortex size was found to increase with time as predicted. This vortex size was measured from a distribution of vortex sizes which showed a distinct peak at some average size and which was identified as the typical length scale of the flow. The identification of vortex sizes was made by visualizing the flow with particles floating on the film. This is shown in figure 3 which displays a succession of photographs taken at different times after the passage of the grid.

The contours of the vortices marked by the floating particles clearly increase with time. The vortex size distributions showed that, as time elapses, the width narrows while its mean value increases to larger sizes. This behaviour is shown in figures 4(a)–(c) which displays this size distribution for different times after the passage of the grid. A plot of the vortex size versus time shows a linear dependence, as seen in (d). As mentioned in section 1, this increase is in line with Bachelor's prediction.

Couder [2,3] attributes the saturation at long times to the finite size of the frame supporting the soap film. This saturation can also be due to the drift of the film thickness or a damping due to the surrounding air. Bachelor uses a dimensional argument for a linear increase with time, of the characteristic scale  $R$  during the decay of 2D turbulence [17]. It is supposed that, during the decay phase, energy is invariant, so that the properties of the decay depend only on the initial energy and time. This is the origin of the linear relation between the characteristic scale of the turbulence and evolution time. More recent experiments, discussed below, confirm this behaviour [31].

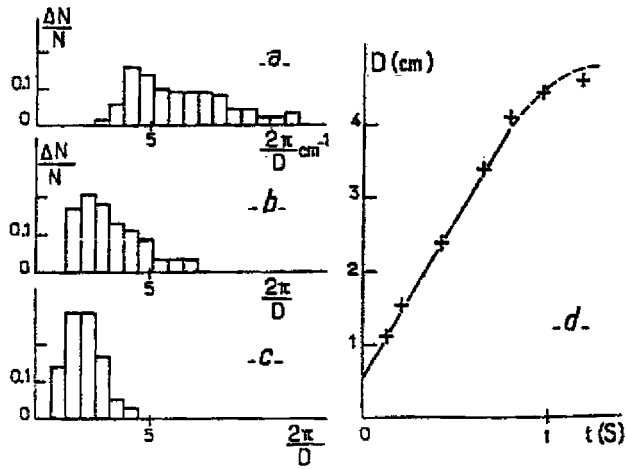


**Figure 4.** (a)–(c) Histograms for the wavevectors  $k = 2\pi/D$  corresponding to times: (a)  $t = (0.12 \pm 0.05) \text{ s}$ , (b)  $t = (0.42 \pm 0.07) \text{ s}$ , (c)  $t = (0.60 \pm 0.07) \text{ s}$ , (d) evolution of the average vortex diameter with time.

**3.1.1. A note on the hydrodynamics of soap films.** In a later study of the hydrodynamics of soap films, Couder *et al* [20] and later Chomaz and Cathalau [21] presented a model that takes into account the thickness variations of the film and its coupling to the velocity field. These variations are accounted for by adding a term to the equations of motion which depends on the gradient of the thickness and the surface elasticity of the film. This modification allowed the authors to interpret the thickness variations as reflecting local pressure variations. The local variation of  $h$  can also be created by a centrifugal force resulting from in-plane variations of the vorticity. The magnitude of these effects will depend on the physical parameters, such as surface elasticity or the time constant, for the exchange of surfactant between the interstitial water and the surfactant layers.

Because the thickness fluctuates, the 2D density of the fluid, which is proportional to  $h(t)$ , varies as well, implying that it is two-dimensionally compressible. The speed  $c$  of the peristaltic ‘sound waves’, associated with this compressibility, is of the order of several  $\text{m s}^{-1}$ , which is much larger than the velocity variations  $\delta v$  associated with the vortices, which is in the range of  $\text{cm s}^{-1}$ . Thus the film is effectively incompressible. (Likewise, air can be regarded as incompressible in all subsonic turbulence studies.)

### 3.2. Forced turbulence in thin layers of fluid on solid substrates

Sommeria carried out one of the earliest studies of quasi-2D flow using a thin layer of conducting fluid on a solid substrate to study the inverse cascade [1]. In this experiment, which falls into the category of steady forced 2D turbulence, the flow of a horizontal layer of mercury contained in a closed square box is electrically driven, while the 3D perturbations are suppressed by means of a vertical magnetic field. The flow field is characterized by measuring the stream function which is proportional to the electric potential. Flow visualization by particles floating on the surface show that the flow takes the form of a regular array of vortices at low currents while a transition to a turbulent state is obtained at higher currents.

Figure 5 shows the set-up: a square box, roughly 12 cm on a side, contained a layer of mercury having a thickness of 2 cm. The box is placed in a vertically directed dc magnetic field of magnitude smaller than 1 T. Two configurations are used: in the first one, the surface

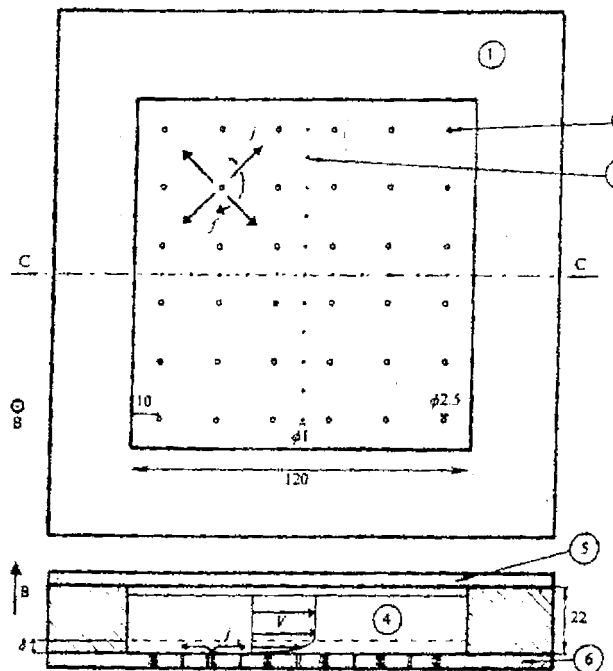


**Figure 5.** The apparatus: the current distribution near one electrode and the velocity profile are schematized. The Hartmann layer depth is denoted by  $\delta$ . (1) Copper frame. (2) Electrodes for current injection and electric potential measurements. (3) Electrodes for electric potential measurements only. (4) Mercury. (5) Glass cover. (6) Electrically insulating bottom plate in which electrodes are embedded.

of the mercury is free and in contact with pure nitrogen to minimize oxidation of the surface; in the second, the surface is rigid due to the formation of an oxidation layer. The flow velocity is kept small to minimize surface height variations. A square array, consisting of 36 equally spaced electrodes placed at the bottom of the box, provide the electric current driving the flow. The current could be varied up to 20 A.

The surface of the mercury is decorated with floating particles, and their motion is tracked photographically. In addition, the local electric potential is measured, allowing for a more precise determination of the flow field. A set of eleven equally spaced electrodes for the measurement of the electric potential were placed in the middle of the box in the two orthogonal directions. An interesting property of the measured potential is that it is directly proportional to the stream function.

Sommeria argues that, for this type of flow, the layer of mercury can be divided into two parts: a part near the solid substrate (the Hartmann layer) of thickness  $\delta = \sqrt{(\rho v)/(\sigma B^2)} = a/M$ , where  $\rho$  is the fluid density,  $v$  is its viscosity,  $\sigma$  is the conductivity,  $B$  is the magnetic field,  $a$  is the total fluid depth and  $M$  is the Hartmann number. The upper layer, which is above the Hartmann layer, should be 2D, since velocity fluctuations in the vertical direction are heavily damped due to the presence of the magnetic field.

Friction in the Hartmann layer is the main source of dissipation in this experiment. As indicated in figure 5, the velocity profile decreases to zero over a length given by the Hartmann layer thickness; above this layer is another, in which the profile is basically independent of height. Despite the viscous dissipation in the Hartmann layer, the flow field is observed to become turbulent at relatively high driving currents.

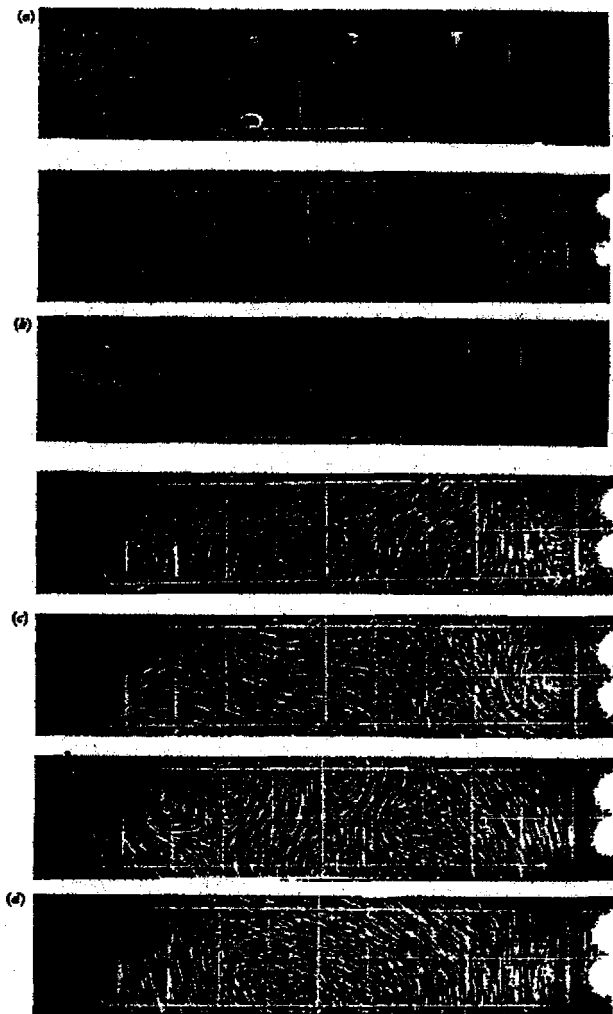


**Figure 6.** Photographs of a central band of the upper surface, using a  $45^\circ$  mirror. The velocity field is represented by the traces of small particles (it is the time of exposure, the scale is 1 cm/division). (a) The initial motion when the current is switched on. (b)  $Rh = 7.27$ ,  $B = 0.48$  T,  $t = 195$  ms (2 examples). (c)  $Rh = 29.1$ ,  $B = 0.24$  T,  $t = 114$  ms (2 examples). (d)  $Rh = 41.1$ ,  $B = 0.12$  T,  $t = 195$  ms (2 examples).

In addition to the Reynolds number, the flow is characterized by a second non-dimensional number  $Rh = s(a/L)^2 Re/M$ , where  $L$  is the box size and  $s$  is a constant equal to 1 for a free upper surface and equal to  $\frac{1}{2}$  for a surface covered with an oxide layer and therefore rigid. The Reynolds number is given by  $Re = (L/v)(BI/\rho a)^{1/2}$ .

The experiments are carried out for variable currents. Sommeria's central observation is that, as the current increases, a transition takes place from an organized array of vortices to a turbulent state at a value of  $I = 1.033A$ , which corresponds to a value of  $Rh = 1.78$ . This transition occurs through the pairing of equal sign vortices, as seen in figure 6. The transition is illustrated in this series of photographs of the flow in a central strip of the box. The images are taken using small particles on the surface as tracers of the velocity. It is apparent that the flow is dominated by coherent vortices.

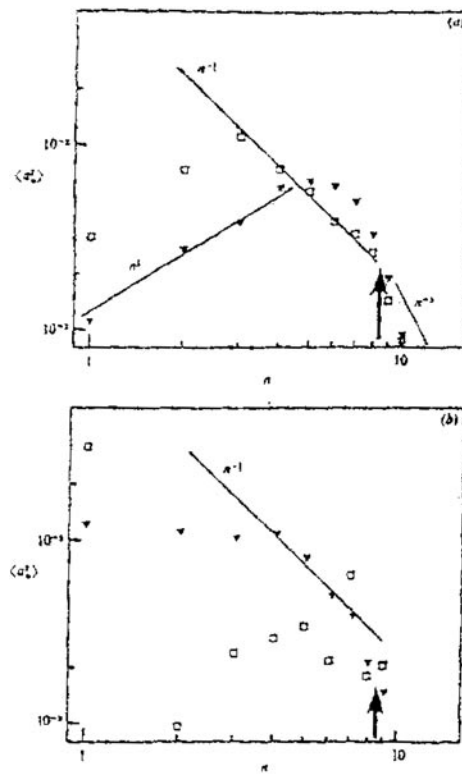


**Figure 7.** One-dimensional spectra of transverse velocity component in log-log coordinates. The points correspond to the first 12 terms of the Fourier series computed from a periodic profile obtained after a symmetrization (see section 2.2). The normalization is such that  $\sum_1^\infty \langle \alpha_n^1 \rangle = 2 \langle r_h^1 \rangle$ . The wavenumber is expressed in units of  $\pi/L$ . The slopes  $-\frac{1}{2}$ ,  $-3$  and  $1$  are indicated as well as the injection wavenumber. (a)  $\nabla Rh = 5.04$  (free upper surface,  $B = 1$  T,  $I = 2$  A);  $\square Rh = 14.24$  (rigid upper surface,  $B = 0.25$  T,  $I = 16$  A); (b)  $\nabla Rh = 27.4$  (free upper surface,  $B = 0.25$  T,  $I = 16$  A);  $\square Rh = 40.3$  (free upper surface,  $B = 0.125$  T,  $I = 16$  A).

A quantitative description of the turbulent state is obtained through measurements of the potential measured along the 11 electrodes which yield the spatial variations of the stream function. Spatial derivatives are taken as finite differences to obtain the transverse velocity from the stream function. After obtaining the spatial variation of the transverse velocity along a line parallel to the set of 11 electrodes, the authors proceed through Fourier transforms to obtain the one-dimensional velocity spectrum which is proportional to the energy density  $E(k)$ . Sommeria's one-dimensional transverse velocity spectra (the  $a_n$ 's are the Fourier amplitudes of the transverse velocity taken along a line joining the electrodes) appear in figure 7. The arrow indicates the scale of injection and the straight line delineates the  $-5/3$  scaling regime. These spectra are found to correspond to an inverse cascade for about half a decade from the injection scale, which is apparently well defined in this experiment up to about a third of the box size.

The author also determines the Kolmogorov constant  $C$  defined by  $E(k) = C\epsilon^{2/3}k^{-5/3}$ . The resulting measurement of  $C$  versus  $Rh$  is shown in figure 8, where one sees that this constant increases from 3 to 7 as  $Rh$  increases. Sommeria attributes the non-saturation of  $C$  at its asymptotic value of 6 to the finite extent of the inertial range, which we recall is about half a decade in wavenumber. Due to low resolution of small scales the enstrophy cascade is not seen in this experiment.

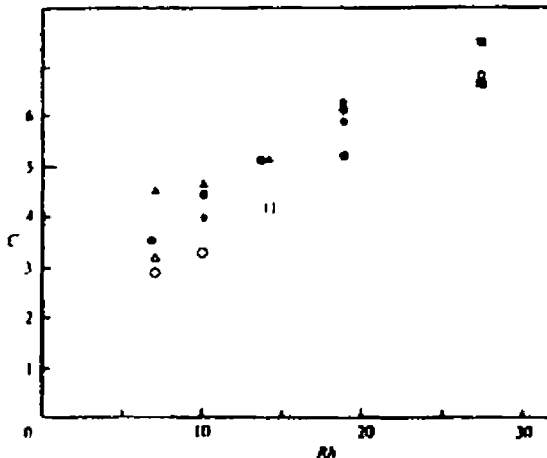


**Figure 8.** Two-dimensional; Kolmogorov constant ' $t$ ' versus  $Rh$  calculated from the spatial spectra. Larger values are an indication of less efficient inverse energy transfers. Free surface:  $\blacktriangle$ ,  $B = t$  T;  $\bullet$ ,  $B = 0.50$  T;  $\blacksquare$ ,  $B = 0.25$  T;  $\star$ ,  $B = 0.150$  T (spectra calculated directly from autocorrelations by (A.8)). Rigid surface:  $\triangle$ ,  $B = t$  T;  $\circ$ ,  $R = 0.50$  T;  $\square$ ,  $B = 0.25$  T.

Several other interesting features were reported in this study: one of the most notable is the onset of a global rotation of the fluid. The sense of rotation can switch randomly. The author attributes this global rotation to the accumulation of energy in the lowest mode of the system which is set by the dimensions of the experimental cell. This observation is in line with the possibility invoked by Kraichnan [10–12] that the inverse cascade can give rise to a sort of Bose–Einstein condensate where the energy is concentrated in the lowest mode of the system. Evidence of such a condensation has also been obtained in numerical simulations [5].

In summary, the above studies of magnetoelectrically generated turbulence in thin layers and turbulence in soap films establish that 2D hydrodynamics and turbulence can be realized in the laboratory, even though the thin layers are viscously coupled to the air or to the walls of the container holding the fluid.

#### 4. More recent work

Soap films are now being used to obtain 2D grid turbulence where the soap film is made to flow at speeds of a few metres per second, giving the advantage of reaching relatively high Reynolds numbers. The flowing soap films can last for several hours without breaking, allowing the experimentalist ample time to make measurements of several quantities characterizing the turbulent flows. Both decaying turbulence and forced turbulence have now been studied in a systematic way. Work on thin layers of fluids has also been extended to study both the decay of turbulence and the velocity fluctuations and their statistics in forced turbulence. In what follows we will first present the experiments done using soap films. Then we will present work on thin layers of fluid on solid substrates.

##### 4.1. Flowing soap films: decaying and forced turbulence

**4.1.1. Soap film tunnel.** In this work, a novel soap film tunnel is introduced to drive the soap film into motion [25]. Recall that in the experiment of Couder the cylinders were towed through a still film to produce grid turbulence and observe its decay. In the experiment of Gharib and

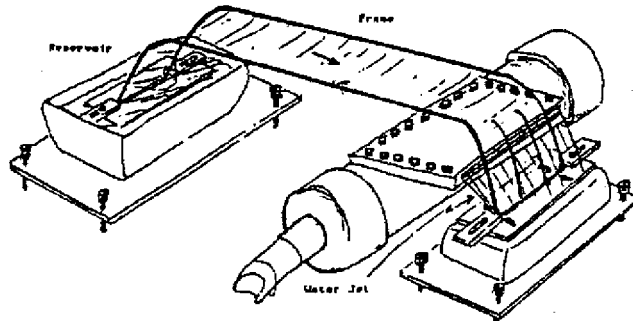


**Figure 9.** Schematics of the soap film tunnel.

Derango (G&D), the new set-up allowed them to set the film itself into motion, enabling observation of the wake behind different objects that penetrate the film. As in Couder's experiments, G&D show photographs of the destabilization of the initial laminar flow by different methods: cylinders generate von Karman wakes, jets give quite a random flow, and grids give rise to a number of vortices interacting to generate turbulence. The visualization of the flow is again interferometric. With this experimental arrangement, the film is long-lived because it is constantly replenished, avoiding a steady decrease in its average thickness.

A schematic of the set-up is shown in figure 9. The channel frame has a flat middle section and is supported by legs which dip into the reservoir of soap solution at one end and are near the film pulling part at the other end. The frame is formed from either glass or copper rods. Typically, the frame width and length were 10 and 30 cm, respectively (see figure 9). The film is drawn from the soap reservoir to the reservoir at the other end. At this end the film is brought into contact with a water jet used to pull the film and drive it into motion. The authors report that the film can last for periods close to 1 h and can be driven at speeds close to  $50 \text{ cm s}^{-1}$ . Flow visualization, as in Couder's experiments, is carried out by illuminating the film in white light and photographing the colourful interference fringes produced by the thin film.

G&D use laser Doppler velocimetry (LDV) for the first time to measure the velocity of the film. LDV is a standard nonintrusive optical technique for the measurement of velocity fluctuations as well as the mean flow speed  $\bar{V}$ . This technique uses a laser beam which is split into two using a beam splitter. A lens converges the two beams to a small spot, forming a fringe pattern at this intersection. The fluid is seeded with small particles that scatter light; when the particle goes through a bright fringe, it scatters light towards the detector. The scattered signal is therefore modulated at a frequency directly proportional to the local velocity. Using appropriate filters, the frequency of modulation can be extracted rapidly and converted to a local velocity.

The shedding frequency behind cylinders is measured as a function of cylinder diameter  $D$  and the mean flow speed  $\bar{V}$ . As fluid flows past a cylinder, a vortex street is obtained downstream of the obstacle. The local velocity component transverse to the mean flow is observed to be a periodic function of time with its power spectrum very sharply peaked at a characteristic frequency to be called  $f_s$ . Measurements in 3D flows show that  $f_s$  is related to  $D$ ,  $\bar{V}$  and the Reynolds number  $Re = \bar{V}D/\nu$ .

From measurements of  $f_s$  for rods of different  $D$ , and  $\bar{V}$ , G&D obtain results that are consistent with measurements of  $f_s$  in 3D experiments (near the onset of vortex shedding, the flow is found to be almost 2D in 3D). To get a good fit, however, they must adjust the viscosity  $\nu$  in  $Re$ , and find it to be larger than that of pure water, even though the soap solution in these

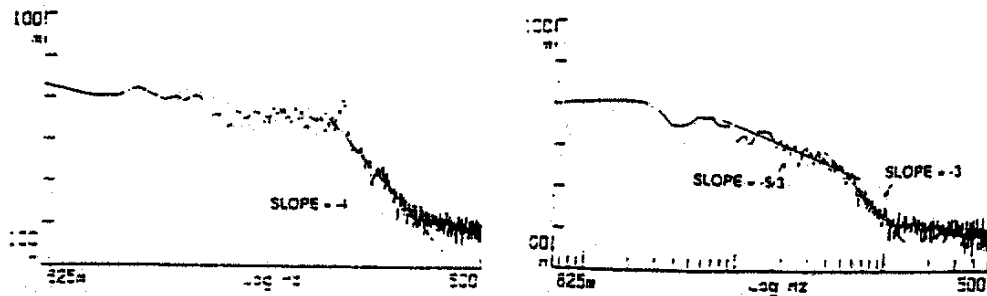


**Figure 10.** The velocity fluctuation spectrum corresponding to generated flow at  $x/m = 43$ .

experiments is extremely dilute. The viscosity of these films is notoriously difficult to measure and may depend on the thickness of the film. Only a few attempts have been made so far; the values reported range from 2 to 10 times the kinematic viscosity of water  $\sqrt{\alpha}$  [55].

A preliminary study of the spectra of longitudinal velocity fluctuations downstream from a grid and a jet is presented by G&D. The results, obtained with LDV, show evidence that turbulence is produced in this channel using grids or jets. The power spectra of the longitudinal velocity fluctuations behind the jet and the grid are clearly broad band as shown in figure 10 and give some evidence of both an energy cascade and an enstrophy cascade as well as a steeper  $-4$  scaling seen at locations near the grid. Note that in this experiment (and in many experiments in 3D turbulence and 2D turbulence to be presented below), the velocity is measured as a function of time at a single point. This time series of the velocity fluctuations is Fourier transformed to obtain the power spectrum as a function of the frequency  $f$ . The frequency  $f$  is then converted to an inverse length scale  $k_y$  along the direction of the flow by invoking the Taylor hypothesis and using  $k_y = 2\pi f/\bar{V}$ .

The Taylor hypothesis, otherwise known as the frozen turbulence assumption, states that the small-scale eddies are being swept by the mean flow past the point of observation without suffering much change. After converting frequency to an inverse length scale, one can compare the results of these one-dimensional spectra to the theoretical predictions of the energy spectrum. The measured one-dimensional spectra can be related to  $E(k)$  in the case where the turbulence is isotropic. If the 1D spectrum decays in a power law form, the exponent is directly related to the exponent of the energy spectrum, as discussed in section 2.2.

**4.1.2. Vertical soap film channel.** The use of soap films to conduct experiments in 2D hydrodynamics is further extended in a study by Kellay *et al* [26]. The film flow is gravity driven in this set-up, with the vertical speed  $\bar{V}$  being as large as  $400 \text{ cm s}^{-1}$ . The film is robust and can last for several hours without breaking, which allows ample time to make measurements with low statistical fluctuations.

The channel consists of an upper reservoir filled with soapy water (a mixture of water and commercial detergent at a concentration of a few per cent) and a lower reservoir; the two being connected by two parallel vertical wires separated by a fixed distance of 5 cm. Wider frames can also be used at the expense of some wobbling of the film due to small air currents. The wires were attached to the floor of the upper reservoir and were weighted at the bottom end in such a way that the weights were suspended in the lower reservoir. A series of five small diameter holes was drilled at the bottom of the upper reservoir along the segment separating the two wires attached to the reservoir floor. Through these holes soapy water drips slowly to replenish the film that is drawn between the two parallel wires.

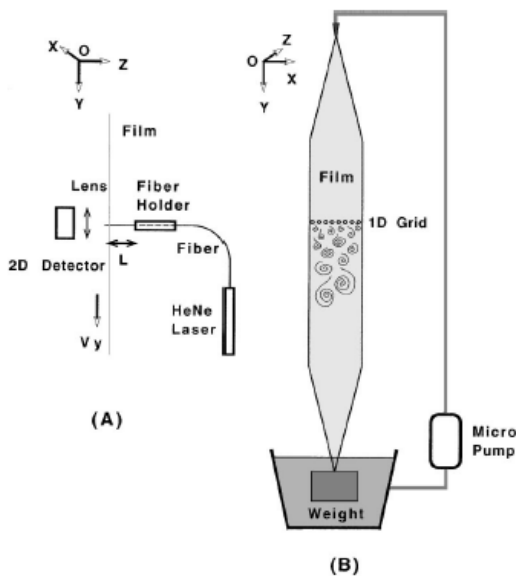


**Figure 11.** (a) A schematic of the fibre set-up. The fibre penetrates the film for less than 0.5 mm and its length measured from the fibre holder is 6 mm. (b) A schematic of the soap film channel set-up. Using a micropump the film is constantly replenished with soap solution. The frame of the channel is nylon wire of diameter 0.08 cm. The width of the channel was 6 cm and its length is 200 cm.

The total channel length used is about 2 m. The injection flux of soapy water feeding the film is controlled both by the level of solution in the upper reservoir as well as by the radius and number of holes.

By varying the level of solution in the upper reservoir, the velocity of the film could be varied between 40 and 400 cm s<sup>-1</sup>. Through a measurement of the flux into the lower reservoir and a measurement of the average velocity of the flow (using LDV), one can obtain an estimate of the mean film thickness; in the experiments of [26],  $h$  was measured to be roughly 5  $\mu\text{m}$ .

This design of soap film channel described above has been considerably refined; later one injection point was used instead of several holes (see the schematic in figure 11). This allowed one to obtain a laminar flow [27]. By inserting a grid through the film, isotropic turbulence could be produced.

The turbulence behind the grid was studied by two methods: homodyne photon correlation spectroscopy (HCS), a method developed for the study of turbulence in three dimensions [28] and which has been adapted to study 2D turbulence, and optical fibre velocimetry (OFV). The latter technique was developed for the purpose of this study [26, 29].

*Velocity differences.* With HCS one can measure the ensemble average of instantaneous velocity differences

$$\delta v_q(\mathbf{r}, t) \equiv v_q(\mathbf{x} + \mathbf{r}, t) - v_q(\mathbf{x}, t), \quad (21)$$

where  $v_q$  is the component of velocity difference along the light scattering vector  $\mathbf{q}$ , its direction chosen by the experimenter [28]. With this scheme, as in LDV, the fluid is seeded with small particles which follow the flow and scatter coherent light from a laser beam. The magnitude of the scattering vector  $\mathbf{q}$  is given by

$$q = 4\pi/\lambda \sin(\theta/2),$$

where  $\lambda$  is the wavelength of the incident beam in the fluid and  $\theta$  is the scattering angle. The method is closely related to LDV, which measures velocities as opposed to velocity differences.

The HCS method requires seeding the fluid with small particles that scatter light from a coherent source, typically an argon laser. The typical diameter for the seed particles might be  $\phi = 0.1 \mu\text{m}$ . For the soap film experiments, the coherent laser beam is split into two parallel beams, which are mildly focused on the film. The separation  $r = l$  of the beams is an adjustable parameter. The two spots were oriented in the horizontal direction so  $r$  was in the transverse direction.

In this experiment, the two incident beams were at about  $45^\circ$  with respect to the film plane; the photomultiplier collecting light from both spots was placed on the opposite side such that the scattering angle was  $90^\circ$ . The scattering plane was horizontal with the scattering wavevector perpendicular to the flow direction. The time variations of the scattered light intensity  $I(t)$  collected by the photomultiplier is sent to a device which directly extracts the autocorrelation function of the light intensity defined as

$$g(t) = \langle I(t' + t)I(t') \rangle / \langle I(t') \rangle^2.$$

The brackets denote an average over  $t'$ .

The function  $g(t)$  is directly related to the properties of the velocity increments of the turbulent flow in the direction of the scattering vector. Since  $q$  was set in the direction transverse to the flow in this experiment, it is the transverse velocity component that was studied.

The intensity correlation function can be written as  $g(t) = 1 + aG(t)$ , where  $a$  is a constant equal to or less than unity, and

$$G(t) = \int P(\delta v(l)) \cos(q\delta v(l)t) d\delta v(l).$$

Here  $\delta v(l)$  is the velocity difference between the two illuminated spots on the flowing soap film and  $P(\delta v(l))$  is the probability distribution of the velocity increments between points separated by  $l$ .

One can show [28] that if

$$\delta v(l) \sim l^\alpha,$$

then  $G(t)$  is likewise self-similar:

$$P(\delta v(l)) = Q(\delta v(l)/\overline{\delta v(l)})/\overline{\delta v(l)}, \quad (22)$$

with

$$\overline{\delta v(l)} \propto l^\alpha, \quad G(t) = G(q\overline{\delta v(l)}t) = G(ql^\alpha t). \quad (23)$$

The exponent  $\alpha$  can be determined by rescaling the time axis as  $tl^\alpha$  and varying  $\alpha$  to make the different  $G(t)$  collapse onto the same curve. From the above expression, it is apparent that the HCS scheme measures only the symmetric part of the full probability density function. Expansion of  $\cos(q\delta v(l)t)$  in the expression for  $G(t)$  shows that it yields only the even moments of  $\delta v(l)$ .

Figures 12 and 13 show an approximate self-similarity of velocity differences as measured in a turbulent, flowing soap film [26]. Identifying a characteristic velocity difference  $\overline{\delta v(l)}$ , with the  $1/e$  decay time  $\tau$  of  $g(t)$  by setting  $q\overline{\delta v(l)}\tau = 1$ , then a plot of  $1/\tau$  versus  $l$  should exhibit a slope that is approximately unity in the enstrophy cascade range of 2D turbulence, according to equation (9) (in the inverse cascade range one would expect  $1/\tau \propto l^{1/3}$ ). The data in figure 13 show roughly a slope of unity in the limited interval  $0.2 < l < 0.4 \text{ cm}$ .

The data in figure 12 offer a direct test of self-similarity of  $g(t)$  and  $P(\delta v(l))$ . If  $g(t) = g(qt\overline{\delta v(l)})$  and if  $\overline{\delta v(l)} \propto l^\alpha$ , the measurements of  $g(tl^\alpha)$ , made at all values of  $l$ ,

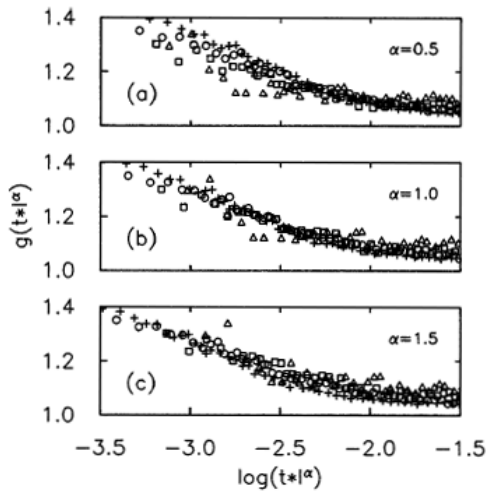


**Figure 12.** Scaling form of the intensity–intensity autocorrelation function. The data have been rescaled to  $tl^\alpha$  with  $\alpha = 0.5$  (a), 1.0 (b) and 1.5 (c). The scattering volume was at  $Y = 0.5$  cm below the comb with  $M = 0.1$  cm, and the mean flow velocity was  $1 \text{ m s}^{-1}$ . Here  $l$  is 0.4 cm (triangles), 0.29 cm (squares), 0.19 cm (circles), and 0.14 cm (crosses).

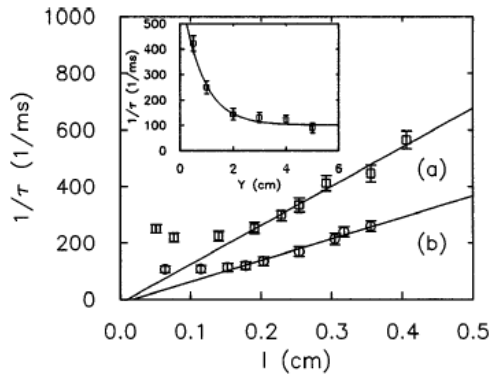


**Figure 13.** Inverse decay time  $1/\tau$  as a function of length scale  $l$ . Curves *a* and *b* are for scattering volume at  $Y = 0.5$  and 2.7 cm below the grid, respectively. The mean velocity of the flow is  $1 \text{ m s}^{-1}$ . Inset:  $1/\tau$  for fixed  $l = 0.28$  cm and for different distances from the comb with  $M = 0.1$  cm.

will lie on a single curve. The four sets of measurements show the best collapse for  $\alpha = 1.0$ , again suggesting that the measurements are in the enstrophy range of 2D turbulence; scaling is absent with  $\alpha = 1/3$ , which is the 2D inverse cascade and 3D value.

By taking the cosine transform of  $g(t)$ , one directly determines the (symmetric part of the) probability density function,  $P(\delta v(l))$ . In principle, of course, a knowledge of  $P$  is sufficient to obtain all even moments of the component of  $\delta v(l)$  along the experimentally chosen direction of  $q$ . In actuality, the HCS scheme is not a good one for extracting the higher moments. However, it does yield valuable information about the shape of  $P$  over a rather wide range of scales  $l$ . The HCS experiments discussed above show that  $P$  is far from Gaussian in this experiment; it is better fitted to an exponential form out to values of  $\delta v(l)$  that are several times the width,  $\delta v(l)$ , of  $P(\delta v(l))$ .

*Energy spectra.* The existence of an enstrophy cascade suggested by the HCS measurements is corroborated by measurements made with a new type of velocimeter. Recall, first, that if the turbulence is self-similar, then  $S_2(R)$  and  $E(k)$  are simply related. Writing

$$E(k) \sim k^{-b}$$

and assuming that  $S_2(R) \sim R^{\zeta_2}$ , then dimensional arguments imply that  $b = \zeta_2 + 1$ . Translating the Kolmogorov–Kraichnan argument for 2D turbulence from coordinate space  $R$  to momentum space  $k$  (see section 2.2), one has

$$\begin{aligned} b &= 5/3 & k < 2\pi/r_{\text{inj}} \\ b &= 3 & k > 2\pi/r_{\text{inj}}. \end{aligned} \quad (24)$$

Spectral data reported here were made with the optical fibre velocimeter [26]. The principle of the OFV is simple: the flowing film and the velocity fluctuations in it deflect a very thin optical fibre (typically 50  $\mu\text{m}$  in diameter). The fibre penetrates the film a distance less than 0.5 mm. It is clamped at a distance of a few millimetres from the film and its far end is connected to the output of a HeNe laser. The end which penetrates the film emits a somewhat diffuse light beam, and the intensity maximum is measured with a position detector (see figures 11(a)). The horizontal and vertical displacements of the fibre are directly related to the velocity fluctuations of the film, as shown by separate calibrations using LDV [29]. The time trace of the longitudinal and transverse components of the velocity are obtained almost simultaneously in this way.

The Fourier transform of the time series of the fluctuating velocity time series is recorded [26] to determine the power spectra  $S_{xx}(f)$  and  $S_{xy}(f)$  of  $v_x(t)$  and  $v_y(t)$ . If the spectral variable  $\omega$  is replaced by  $\bar{V}k$  (Taylor's hypothesis), and if the turbulence is isotropic, then both spectra are proportional to  $E(k)$ .

The results obtained for the velocity spectra in [26, 32] clearly indicate that the turbulence is isotropic for scales between about 2 mm and a few centimetres (see figures 14 and 15). Generally for scales comparable and larger than the channel width, the spectra for transverse and longitudinal components do not have similar amplitudes and the turbulent flow is anisotropic, but for smaller scales the turbulence is quite isotropic, with the amplitude of the transverse velocity spectrum being very close to the amplitude of the longitudinal component spectrum.

Another conspicuous feature of the spectra is the scaling found at small scales. The spectrum decays in a power law fashion for a range slightly greater than a decade, as seen in figures 14 and 15. The exponent deduced from these spectra depends slightly on the location to the grid and ranged between about  $b = 3.3$  and  $3.7$ . Generally, this exponent is larger near the comb. These exponents are very different from the Kolmogorov exponent  $b = 5/3$ , expected in 3D turbulence and in the inverse cascade range in 2D turbulence (see equation (24)). In the enstrophy cascade range of scales, this exponent is expected to be 3 (see equation (24)), which is consistent with the measurements in figures 14 and 15. Note that spectral measurements made by the HCS and OFV techniques are consistent with the existence of an enstrophy cascade from large to small scales. These results are also in agreement with the previous measurements of G&D discussed above and where an enstrophy cascade like scaling was also found in grid turbulence.

In the soap film experiments discussed so far, there is no sign of the inverse cascade. These quantitative studies are consistent with visual observations; the interferometric snapshots clearly show merging of vortices and some coarsening associated with an increase of vortex sizes. In decaying turbulence, current expectations rule out inverse cascade scaling but point rather to an increase of the integral scale [30]. These results are therefore in agreement with such expectations. Recently, more careful experiments [31], to be described below,

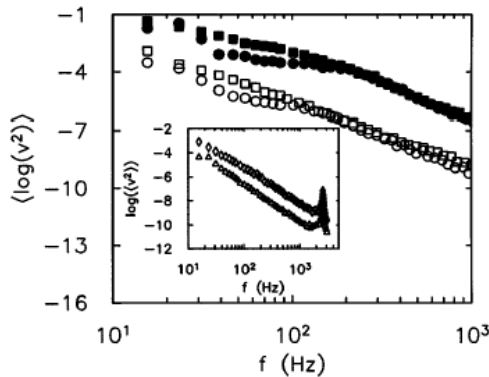


**Figure 14.** Power spectrum of the fibre position fluctuations, or equivalently the velocity fluctuations, measured at a distance of 80 cm from the entrance of the channel. The lower two spectra are for the longitudinal  $S_{yy}(f)$  (open squares) and transverse  $S_{xx}(f)$  (open circles) velocity fluctuations at 4 cm behind a comb with  $M = 0.3$  cm. The upper two spectra are for longitudinal (filled squares) and transverse (filled circles) fluctuations as measured at 1 cm behind a comb with  $M = 0.1$  cm. Inset: spectra in the absence of the comb as measured at a distance of 80 cm from the entrance of the channel. The diamonds are for longitudinal fluctuations and the triangles are for transverse ones. Here  $V = 2 \text{ m s}^{-1}$ . In this inset we display the power spectra out to  $f = 10^4 \text{ Hz}$ , so that the effect of the resonant frequency of the fibre may be seen.

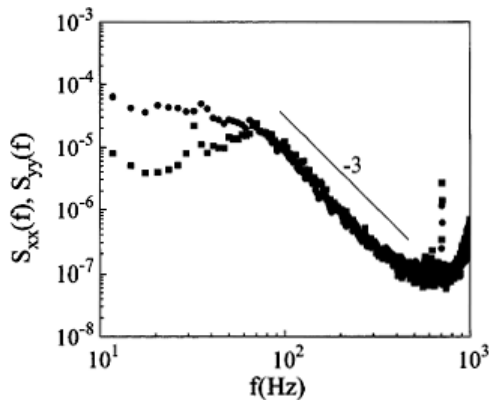


**Figure 15.** Longitudinal (filled circles) and transverse (filled squares) velocity power spectra measured at distance  $Y = 6$  cm below the grid. The flow rate is  $0.6 \text{ ml s}^{-1}$ . Isotropy is clearly seen at high frequency corresponding to small wavelength velocity fluctuations. The line has a slope of  $-3$ .

using these turbulent soap films show that the growth of the integral scale follows theoretical predictions by Batchelor.

*Vorticity spectra.* As a continuation of the study of the properties of turbulence in this soap film channel, the authors developed a novel vorticity meter to measure the instantaneous vorticity fluctuations of the turbulent soap film [32]. To carry out the measurement two velocity probes are used to measure both components of the velocity for two different locations at the same horizontal position. The two OFV probes are separated by a distance of 0.07 cm, fixing the spatial separation  $Dx$  for carrying out finite differences. By measuring these velocities at time  $t$  and time  $t + dt$ , one can invoke the frozen turbulence assumption to get a measurement

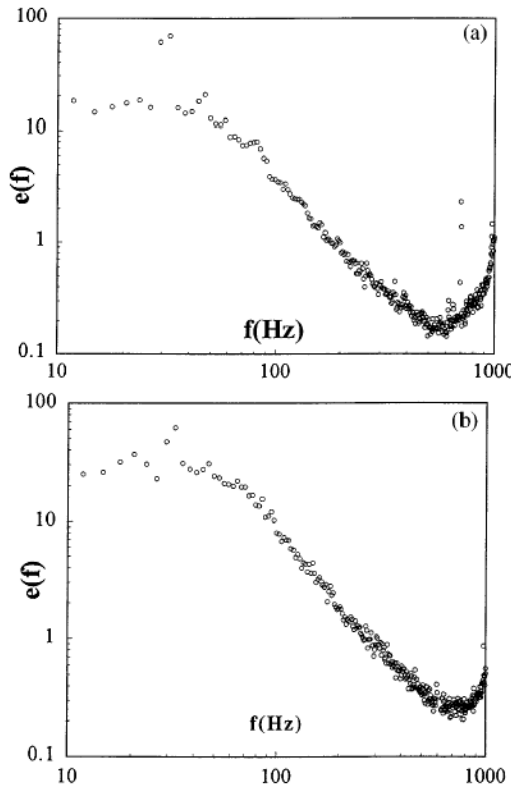


**Figure 16.** (a) Vorticity power spectrum behind a 1D grid measured at  $Y = 5 \text{ cm}$  and with a flow rate of  $0.68 \text{ ml s}^{-1}$ . (b) Vorticity power spectrum measured at  $Y = 7 \text{ cm}$  and with a flow rate of  $0.75 \text{ ml s}^{-1}$ .

of the velocity at two other locations separated vertically from the position of the probes by  $Dy = V dt$  such that  $Dx = Dy$ . In this way the two components of the velocity are obtained in four different points.

Using the above scheme, measurements of the vorticity fluctuations are obtained from finite differences [32]. Advantage is taken of the two-dimensionality of the flow since the vorticity vector has only one significant component; the two others in the plane of the film are heavily damped by viscosity. The other advantage is provided by the use of the fibre velocimeter which allows almost simultaneous measurements of the transverse and the longitudinal components of the velocities at the different points, allowing the use of finite differences to approximate the velocity gradients.

The measurements in [32] focused on the power spectrum of the vorticity fluctuations. These power spectra were measured behind grids at locations where the turbulence was relatively isotropic for scales between about 2 mm and 4 cm. Typical vorticity power spectra and the corresponding velocity spectra are shown in figures 15 and 16 at a location of 5 and 7 cm from the grid and a flux of  $0.75 \text{ ml s}^{-1}$ . The mean speed of the flow is approximately  $2 \text{ m s}^{-1}$  and the mean thickness is about  $7 \mu\text{m}$ . The vorticity spectra are seen to be broad band and become flat at frequencies below about 50 Hz. Since  $k = 2\pi f/V$  (frozen turbulence assumption), this frequency corresponds to a scale of 4 cm, which is comparable to the channel width fixed at 6 cm. The spectrum then decays at higher frequencies from about 60 to 600 Hz; this decay can be approximated by a power law of the form  $e(f) = \langle \omega^2(f) \rangle \simeq f^{-1.8}$ .

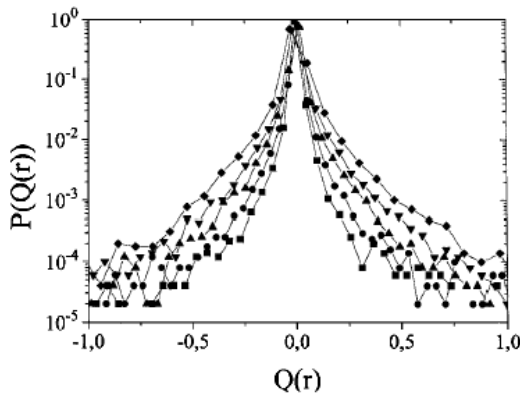


**Figure 17.** Experimental probability density functions for  $\delta u(r)\delta\omega^2(r)$  for different values of  $r$ .  $r = 0.2$  cm (squares),  $0.4$  cm (circles),  $0.6$  cm (up triangles),  $0.8$  cm (down triangles) and  $1$  cm (diamonds). The measurements are carried out at a distance of  $6$  cm from the grid.

The vorticity measurements, together with the frozen turbulence assumption, imply  $e(k_y) \simeq k_y^{-1.8}$ , where  $k_y$  is the wavenumber in the flow direction  $k_y = 2\pi f/\bar{V}$ . According to theories of the enstrophy cascade, the exponent should be  $-1$ ; the exponent measured in this experiment is clearly larger. This discrepancy can be attributed to different factors such as the anisotropy of the flow, the thickness fluctuations of the soap film as they may render it compressible, or to the presence of coherent structures in the vorticity field as flow visualization clearly shows the presence of several large vortices dominating the flow. Another source of error may be the finite difference scheme used which is limited in scope as the distance between probes could not be made small enough to approach the dissipative scale.

*Probability density functions of the enstrophy flux.* Another quantity which was also determined recently is the enstrophy flux in decaying grid turbulence [47]. This flux can be evaluated from measuring the quantity  $Q(r) = \delta u(r)\delta\omega^2(r)$ , where  $\delta u(r)$  is the longitudinal velocity increment while  $\delta\omega(r)$  is the vorticity increment across a longitudinal scale  $r$ . The experiments, which were compared to results from direct numerical simulations of 2D grid turbulence, reveal that the probability density function (PDF)  $P(Q(r))$  is highly non-Gaussian and fits closely to a double-sided stretched exponential with a stretching exponent of  $0.4$ , as shown in figures 17 and 18 where both the experimental data and the results of the numerical simulations are plotted.

The PDFs measured for different values of  $r$  in [47] can be made to collapse onto a single curve by simply rescaling the  $Q$  axis as  $Q/r$  (figure 19), which leads to the conclusion that the moments of  $Q(r)$ ,  $\langle Q^n(r) \rangle$ , should scale as  $r^n$ . Measurements of the absolute first moments of  $Q(r)$  confirms this dependence as it turns out to be linear in  $r$  for a range of scales between  $0.2$  and  $1.5$  cm. This linearity of the absolute first moment could be anticipated from an exact relation in 2D homogeneous turbulence, namely  $\langle Q(r) \rangle = -2\beta r$  [19]. These findings therefore point to the fact that the enstrophy transfer rate  $\beta$  is constant in 2D decaying grid turbulence.

**4.1.3. Second, third and fourth moment measurements and a test of the Taylor hypothesis in vertical soap films.** Belmonte *et al* [9] have also carried out a series of experiments on the velocity structure functions, focusing on the third moment of velocity differences in these rapidly flowing soap films [9]. The soap film channel used is similar to the one in the previous

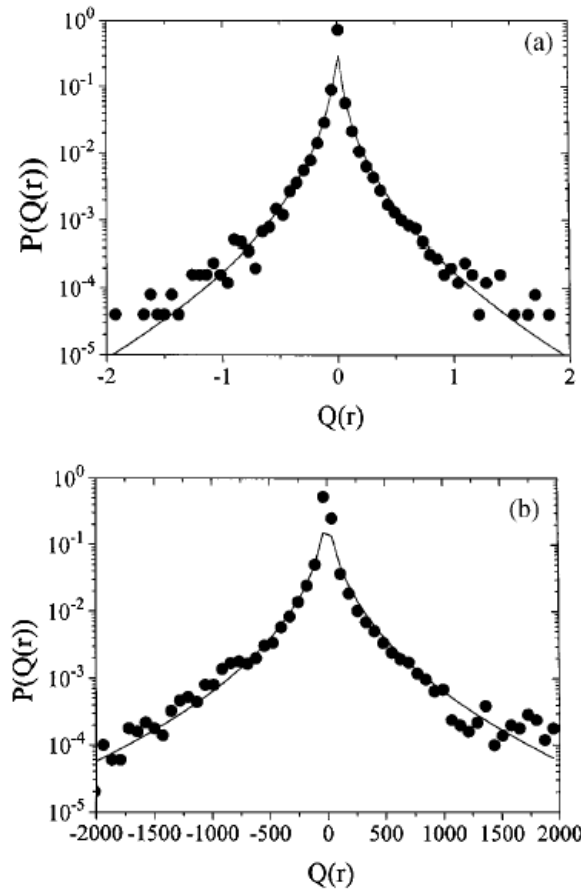


**Figure 18.** (a) Experimental PDFs for  $\delta u(r)\delta\omega^2(r)$  and a fit using a stretched exponential function with an exponent of 0.41 ( $r = 1 \text{ cm}$ ). (b) PDFs for  $\delta u(r)\delta\omega^2(r)$  from the numerical simulations for a Reynolds number ( $Re$ ) of  $5 \times 10^5$  ( $r = 0.06 L$ ) along with a stretched exponential fit with an exponent of 0.4.

section: a gravity driven soap film using one injection point as in the experiments of [27]. The velocity fluctuations in the longitudinal ( $y$ ) direction are measured using an LDV technique which was described previously. In these measurements, the Taylor hypothesis (which has been shown to work adequately in these soap film experiments, as we will see below [45]) is used to extract the velocity differences across a scale  $r$ . The interpretation of this experiment hinges on the recognition that this is a decaying turbulence experiment.

In addition to measuring the lower moments of  $P(\delta v(r))$ , its functional form at various values of  $r$  was also measured in [9]. While these PDFs seem to show exponential tails for very small scales, they become Gaussian at larger scales as can be seen in figure 20. This figure also shows a spectrum of the velocity fluctuations obtained using LDV; the results are in good agreement with the fibre spectra shown above. The third moment of longitudinal velocity increments, shown in figure 21 (closed circles), starts out small and is very slightly negative at small scales. It goes through a small minimum and then becomes positive and increasing with increasing  $r$ . This moment goes through a maximum and then decreases to zero at large scales where the asymmetry of the PDF becomes almost zero. The third moment is a measure of the coherence

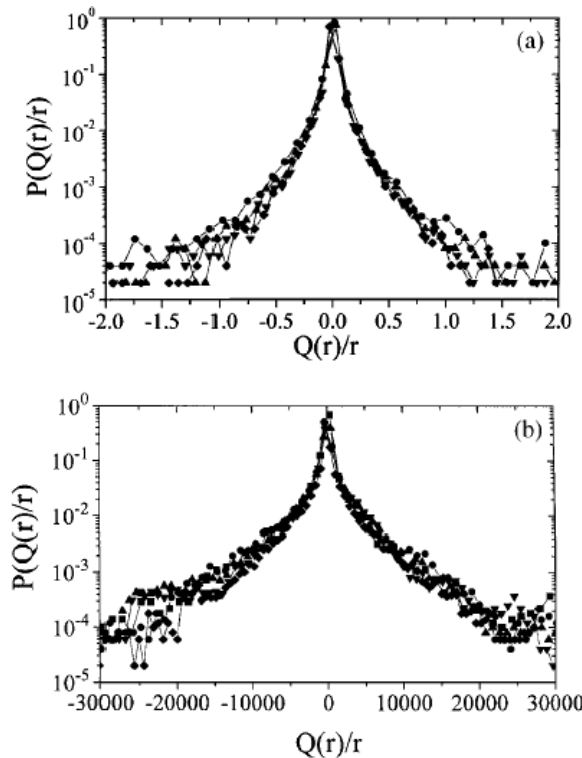


**Figure 19.** (a) Experimental rescaled PDFs for  $\delta u(r)\delta\omega^2(r)$ : the horizontal axis has been divided by  $r$ .  $r = 0.4$  cm (circles),  $0.6$  cm (up triangles),  $0.8$  cm (down triangles) and  $1$  cm (diamonds). (b) Rescaled PDFs for  $\delta u(r)\delta\omega^2(r)$  from the numerical simulations ( $Re = 5 \times 10^5$ ): the horizontal axis has been divided by  $r$ .  $r = 0.05 L$  (squares),  $0.095 L$  (circles),  $0.14 L$  (up triangles),  $0.185 L$  (down triangles) and  $0.23 L$  (diamonds).  $L$  is the channel width.

of velocity differences on scales  $r$  and hence must vanish when  $r$  greatly exceeds the outer scale of the turbulence beyond which  $P$  must become Gaussian by the central limit theorem.

The most notable finding is that the third moment of longitudinal velocity differences  $S_3(r) = \langle \delta u^3(r) \rangle$  is positive, in stark contrast to 3D turbulence, where the measured and the predicted third moment is negative; this relation (equation (6)) is known as the  $-4/5$  law and was derived exactly by Kolmogorov in the 1940s.

Because the turbulence decays downstream from the array of cylinders (comb) that create it, the correlation length increases. This increase contributes a positive term to the expression for the third moment which dominates in the flow configuration studied here. Taking the measured decay of  $J(r, t) = \langle v_y(r_{x+r}, t)v_y(r, t) \rangle$  into account in the exact theory for  $S_3(r)$  [9], one can calculate this function and compare it with the measurement of  $S_3(r)$  itself. The result appears as the full curve in figure 21. The agreement between the two curves is satisfactory, considering that the effect of air damping and the finite width of the soap film channel have not been taken into account in the calculation of  $S_3(r)$ .

If the turbulence is forced rather than decaying,  $\partial J/\partial t$  is zero, as is  $d\langle v^2 \rangle/dt$ . Now  $\epsilon$  becomes the rate at which the forcing power is converted into heat; it is obviously a positive quantity. In this forced steady-state case,  $S_3(r)$  can be shown to be positive at all  $r$  [5]. In the inertial range,  $S_3(r) = +3/2\epsilon r$  and remains positive at all values of  $r$ .

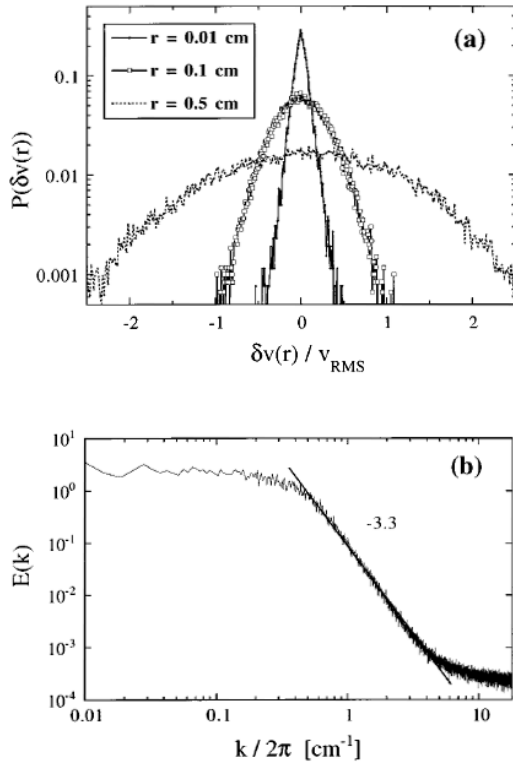


**Figure 20.** (a) The PDFs of  $\delta v(r)$  at the three indicated values of  $r$ . (b) Energy spectrum obtained from the time series of the longitudinal velocity, showing an interval where  $E(k) \sim k^{-3.3}$ . The data in both plots are taken at  $Y = 8 \text{ cm}$ .

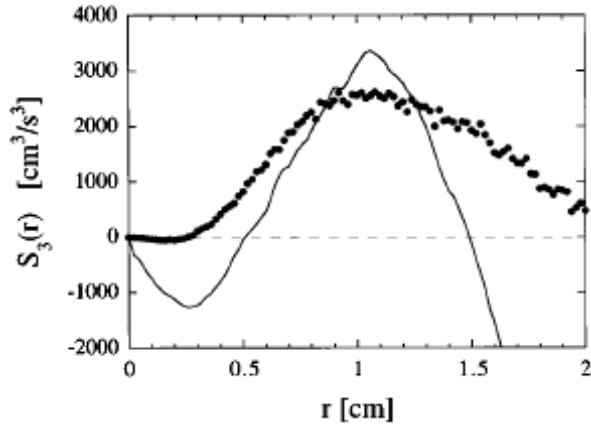


**Figure 21.** The calculated  $S_3(r)$  using the data from figure 5 in equation (5); the full circles correspond to  $S_3(r)$  measured at the same position,  $Y = 8.6 \text{ cm}$ .

In addition to the third moment, second- and fourth-order moments of velocity increments are also measured in [9]. The scaling found by these authors suggest that the second moment scales as  $r^{1.6}$  while the fourth moment scales as  $r^{2.9}$  as seen in figure 22. Recall that the

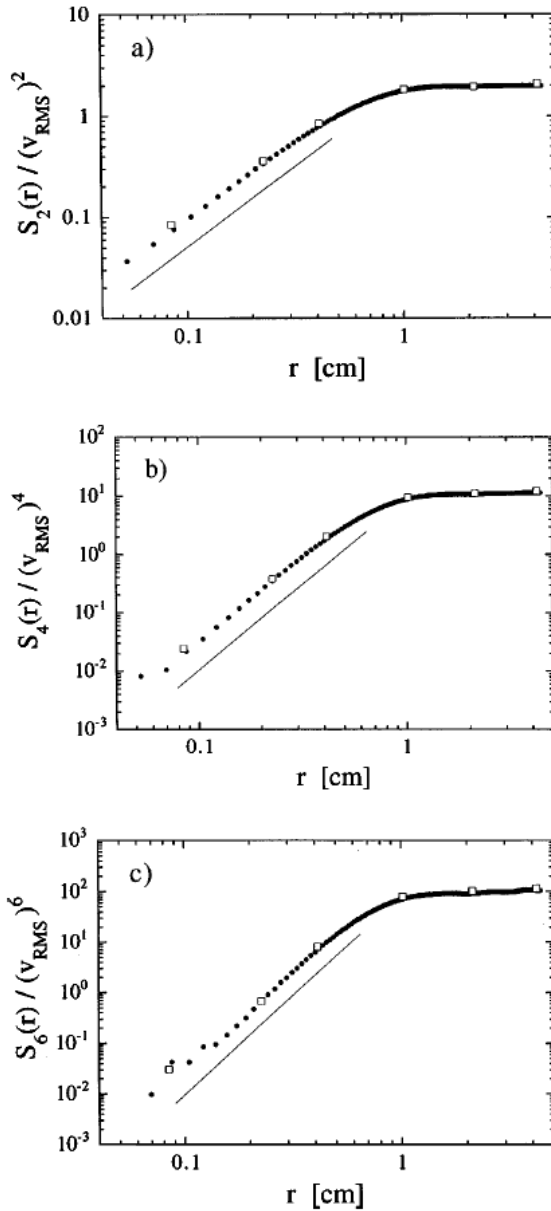


**Figure 22.** Experimental check of Taylor's hypothesis for (a) second-order structure function  $S_2(r)$  taken at  $x = 8$  cm using Taylor's hypothesis; (b) fourth-order structure function  $S_4(r)$ ; (c) sixth-order structure function  $S_6(r)$ . The open squares are direct spatial measurements made using two probes, and the lines correspond to the fitted scalings described in the text.

exponents expected are 2 and 4 for the enstrophy cascade range. The authors argue that the extent of the inertial range is to blame for this deficit.

Belmonte *et al* [45] went further and directly tested the Taylor hypothesis in these soap films by making measurements with two LDV probes in order to measure the velocity at two separated points at almost the same instant in time. The results are shown in figure 22, where the values of  $S_2(r)$  and  $S_4(r)$  measured directly are compared to their counterparts measured using

the Taylor hypothesis. The agreement between the measured values gives a good indication that this assumption works surprisingly well in this system.

One expects that the difference between forced and decaying turbulence should also reveal itself in moments other than  $S_3$  and the underlying probability density function  $P(\delta v(r))$ . Though no rigorous theory exists for these functions, there does exist computer simulations for  $P$  in the forced case. In the inverse energy cascade range, ( $r > r_{\text{inj}}$ ; ( $k < 2\pi/r_{\text{inj}}$ )), the skewness is very small and  $P$  is almost Gaussian in form [42]. Forced turbulence experiments will be discussed below.

**4.1.4. Effects of air drag on turbulence and decay laws.** Martin *et al* [31] have explored the role of air friction on grid turbulence generated in these rapidly flowing soap films driven by gravity. The issue of air drag has been considered by Couder *et al* [20], but no experimental test has been carried out. In [31], LDV is again used as a tool to probe the velocity fluctuations. Air friction is a legitimate concern in the experiments with flowing soap films, as pointed out previously by Couder *et al*, and may present a serious drawback to the use of soap films as 2D test beds since the coupling with air not only introduces an additional dissipative mechanism but also prevents the velocity fluctuations from being strictly 2D. It turns out, however, that air friction affects only velocity fluctuations at such large scales  $r$  that most soap film measurements of  $S_n(r)$  and  $P(\delta v(r))$  apparently do not feel its effect [46].

By enclosing the soap film in a sealed chamber and extracting as much air as possible from the chamber to minimize friction against the surrounding air, Martin *et al* tested the effects of air friction directly through a comparison of the spectral properties of the velocity field at two different pressures. It was found that the shape of the spectra changes little while the amplitude had a tendency to increase as the pressure decreases or as the air friction thereby decreases. The turbulence is still found to be anisotropic at large scales. The exponent  $b$  for the small-scale part was found close to  $-3.3$ , in agreement with previous determinations. A novel feature of these experiments was the decrease observed for the transverse velocity spectrum at large scales. An exponent of  $1.5$  was found, which differs from  $b = 3$ , which was found numerically and suggested theoretically [14, 30]. The spectra are shown in figure 23.

A change in the integral scale  $l_{\text{int}}$  and the rate of its increase as it travels downstream from the grid was evidenced. Martin *et al* [31] tested the growth law for this integral scale as a function of downstream distance, or equivalently as a function of time, and found reasonable agreement with the linear law predicted by Batchelor. The integral scale was extracted from the spectra and was identified as the crossover in the transverse velocity spectrum from  $k^{-3.3}$  to  $k^{1.5}$ . This crossover is indicated in figure 23 and the integral scale versus time is shown in figure 24. The measurements are carried out for different distances  $Y$  from the grid, and time is defined as  $Y/\bar{V}$ . This observed growth of the integral scale is consistent with Couder's earlier observations concerning the growth of vortical structures in the decay of grid turbulence using soap films.

Another quantity measured by Martin *et al* is the average one-component kinetic energy density  $K = 1/2\langle v^2 \rangle$  where  $v$  is the velocity. The kinetic energy is found to be larger at low pressure than at high pressure, clearly indicating that air drag acts as a sink for  $K$ . At both pressures,  $K$  decreases smoothly with time or distance from the grid and shows some signs of levelling off at large times.

**4.1.5. Energy, enstrophy and thickness statistics using particle image velocimetry.** Rivera *et al* [43, 48] have also explored turbulence in flowing soap films using PIV and thickness measurements. Image analysis software was used to track the motion of titanium oxide seed in the soap solution. The film thickness was measured using light transmission by the soap

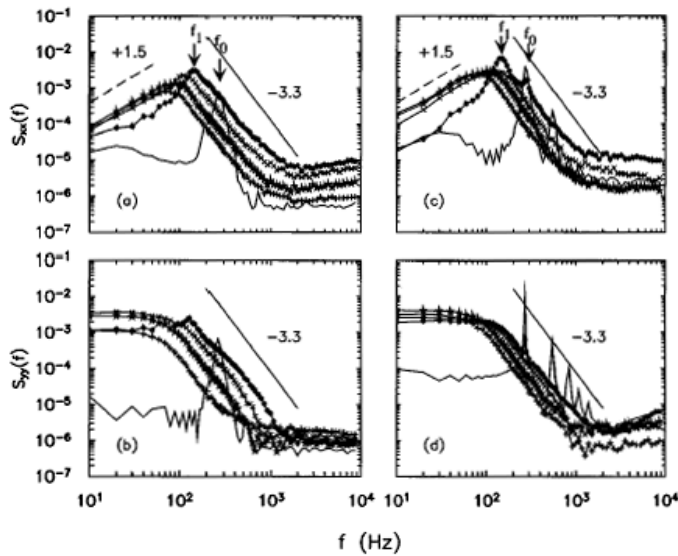


**Figure 23.** Velocity power spectra. The figures on the left, (a) and (b), correspond to measurements at  $P = 760$  Torr while the figures on the right, (c) and (d), correspond to  $P = 45$  Torr. The figures on the top and the bottom are, respectively, the transverse,  $S_{xx}$ , and longitudinal,  $S_{yy}$ , spectra. The full circles, crosses, stars and pluses are for  $Y = 3, 6, 12$  and  $20$  cm, respectively. The full lines without symbols are for  $Y = 1$  cm. At short times (or  $Y = 1$  cm) the spectra consist of sharp peaks, the signature of periodic shedding of vortices due to the grid. The fundamental frequency  $f_0 \simeq 280$  Hz. Following this short-time behaviour is a subharmonic bifurcation which occurs at  $f_1 \simeq f_0/2$ , as is readily seen on the transverse spectra (a) and (c) for  $Y = 3$  cm. For  $Y > 3$  cm the spectra are broad band, consisting of many Fourier modes. On the high-frequency side, all the spectra with  $Y > 6$  cm are consistent with the power-law decay of  $k^{-3.3}$  which is plotted as full lines. On the low-frequency side, the measurements show  $S_{xx} \propto k^{1.5}$ , which are plotted as broken lines.

film, which, for these measurements, was also seeded with titanium oxide particles. One advantage of PIV is that the velocity and vorticity fields are measured in real space. One-point measurements of the temporal fluctuations of, say, the velocity or the vorticity usually require the use of the Taylor frozen turbulence assumption to make comparisons with theory, but not when PIV is used.

The measurements of Rivera *et al* confirmed the findings for the energy spectra  $E(k)$  obtained in the previously described papers. However, they found a smaller exponent for the enstrophy spectrum, which was not measured directly. Measurements of spectra using PIV are difficult because the grids used are too small ( $60 \times 61$ ). Measurements of the decay of quantities such as the energy, enstrophy and the rms value of the thickness fluctuations are reported. The decay of the thickness fluctuations measured by Rivera *et al* is found to be slower than that of the energy and the enstrophy. A strong correlation is found between the thickness and the vorticity, however; this correlation decays quite fast with downstream distance from the grid. These measurements are shown in figure 25. Figure 26 displays the measured second-order velocity structure function  $S_2(r)$ , the second-order vorticity structure function  $\Omega(R)$ , and the enstrophy flux  $Q(r)$ . The observed exponents are 1.6, 0.4 and 1, respectively. The expected exponents are 2, 0 and 1. The exponent  $\zeta_2$  for  $S_2(r)$  is in good agreement with the measurements of Belmonte *et al* [9]. The exponent for the enstrophy flux is also consistent with later measurements by Kellay *et al* [47]. The vorticity structure function

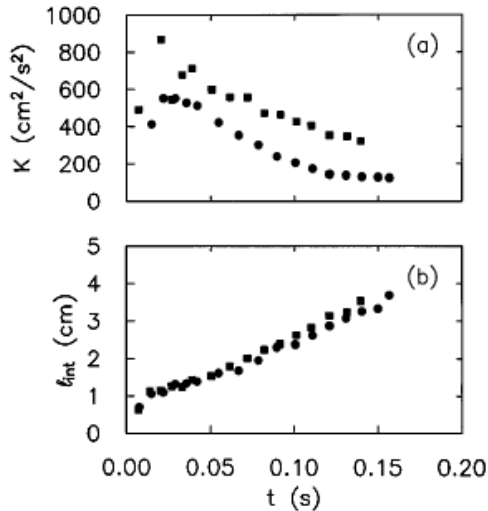


**Figure 24.** (a) Kinetic energy  $K$  and (b) integral scale  $l_{\text{int}}$  versus time  $t$ . Full circles and squares are for  $P = 760$  and  $45 \text{ Torr}$ , respectively. As can be seen at low pressure, the energy  $K$  and  $l_{\text{int}}$  are greater than that measured at high pressure.

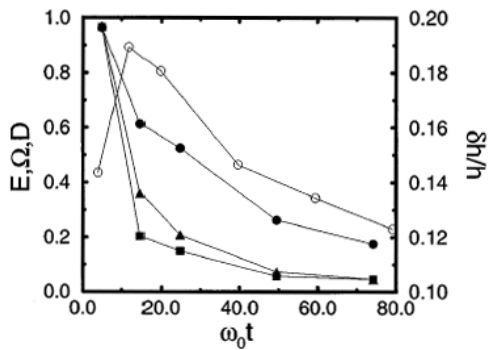


**Figure 25.** Decay of normalized  $E/E_0$  (●),  $\Omega/\Omega_0$  (■),  $D/D_0$  (▲) and  $\delta h/h$  (○) with normalized time  $\omega_0 t$ . Lines are guides to the eye.

gives an exponent which is slightly larger than expected but Rivera *et al* argue that this may be due to the finite difference method used in extracting the vorticity field.

A strong coupling between the vorticity field and the thickness field is reported in [43] and [48] (this effect was anticipated in [21]). The thickness spectra are much steeper than expected: the exponent is  $-2.3$  whereas it would be  $-1$  if the thickness were acting as a passive scalar. The issue of the dynamics of thickness fluctuations in these turbulent soap films seems to remain an open issue.

To what extent is a soap film really 2D, considering that thickness fluctuations are obviously present? Because interference measurements inherently contain a phase shift ambiguity of  $2\pi$ , true thickness measurements, like those mentioned above, are very important. The mean film thickness  $\bar{h}$  and its rms fluctuations  $h_{\text{rms}}$  can be directly measured without this ambiguity by the absorption of a light beam of wavelength  $\lambda = 3 \mu\text{m}$  (water has a strong absorption line at this wavelength). Recent experiments by Wu *et al* show that for a vertically flowing film in a turbulent state,  $h_{\text{rms}}/\bar{h}$  is typically only 5% [22].

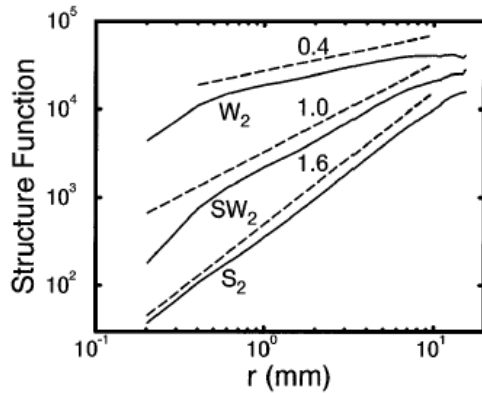


**Figure 26.** Second-order structure functions  $S_2$ ,  $W_2$ , and  $SW_2$  versus  $r$  (full curves) are labelled in the plot. Corresponding slopes are shown as broken curves. For presentation purposes,  $S_2$  and  $W_2$  are scaled by 10 and 0.02, respectively.

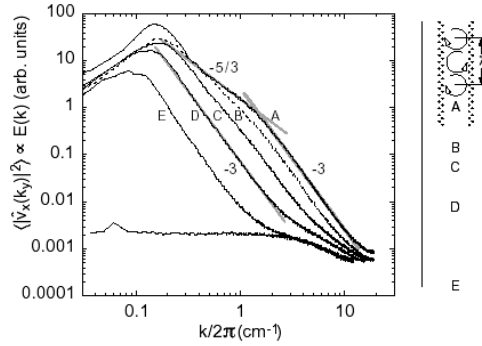


**Figure 27.** Turbulent energy spectra derived from  $v_x(t)$ . From right to left, spectra were measured at positions A–E. The wires bounding the channel were 8 cm apart, the two vertical combs 2.5 cm apart. Downstream distances relative to the ends of the combs are  $A = +5$  cm,  $B = -5$  cm,  $C = -10$  cm,  $D = -20$  cm and  $E = -40$  cm. The bottom curve is a noise background measured for a laminar flow with the combs removed. Grey lines are not fits, but guides to the eye.

**4.1.6. Forced turbulence.** Rutgers has performed an experiment that reveals the clear difference between forced and decaying turbulence in 2D [38]. The turbulence was generated in a vertical soap film channel, as in the experiments discussed above. However, in this study, the horizontal comb was replaced by two almost vertical combs located close to the supporting wires. These combs create forced turbulence between them, much as rough walls would in a 3D water tunnel. A LDV records the horizontal and vertical velocity fluctuations at the lateral mid-point between the supporting wires and at various downstream observation points.

At point A, which lies between the two combs, the turbulence is strongly forced; at points B, C and D increasingly downstream, it is less so. At E, the turbulence should be of the purely decaying type (see the right-hand side of figure 27). At each point, the vertical and horizontal velocity fluctuations  $v_x(y, t)$  and  $v_y(y, t)$  were converted into energy spectra, using the frozen turbulence assumption.

It is quite apparent that at A the spectra in figure 27 exhibit an inverse cascade scaling range at small  $k$  and a direct cascade at large  $k$  (also seen in another configuration as displayed in figure 28). Recall that the spectral exponents in these two regimes are  $b = 5/3$  and 3,

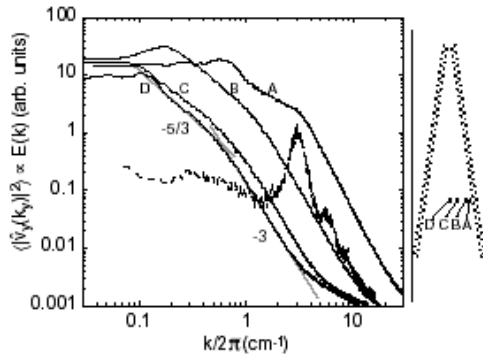


**Figure 28.** Turbulent energy spectra derived from  $v_y(t)$ . From right to left, spectra were measured at positions A–D. The two vertical combs (30 cm long) gradually spread from 2 cm apart at the top to 7 cm apart at the bottom. Cross stream distances relative to the right comb are A—0 cm, B—0.5 cm, C—1.5 cm and D—2.5 cm (which is the channel centre). Turbulence intensities are  $TIA$ —56%,  $TI_B$ —35%,  $TI_C$ —15% and  $TI_D$ —11%. The broken curve was measured 2.0 cm downstream from a single comb tooth. Grey lines are not fits, but guides to the eye.

respectively (see equation (24)). From this figure it is apparent that the dividing  $k$ -value between these two regimes is roughly  $2\pi \times 1.5 \text{ cm}^{-1}$ , which corresponds to an injection scale  $l_{\text{inj}} = 1/(1.5 \text{ cm}^{-1}) = 0.66 \text{ cm}$ . This length is much larger than the tooth diameter of 0.03 cm and the tooth spacing, which was ten times this value. Far below the combs, namely at E, the turbulence is no longer being forced and the spectrum exhibits an enstrophy cascade only, with  $b \simeq 3$ , as in figures 15 and 20.

#### 4.2. Two-dimensional mixing studied with a soap film

Interferometric images of flowing soap films suggest that the thickness variations behave like a passive scalar  $\Phi(x, y, t)$ ; injecting dye near the teeth of a horizontal comb generates patterns downstream that look quite similar to the thickness variations  $h(x, y, t)$  seen in monochromatic light. In the experiment by Wu *et al* [23], discussed next, this connection between  $\Phi(x, y, t)$  and  $h(x, y, t)$  is quantitatively explored.

In this study the soap film is driven into motion with a system resembling a Couette cell but in 2D. Instead of cylinders, very thin disks are used, with a film stretched between them. When the inner disk is set into motion the soap film arranges its thickness to be small near the inner disk and larger near the outer ring. The centrifugal force on the film generates a smoothly varying thickness profile. The constant thickness regions are rings, as can be seen in figure 29(a). This photograph was taken in reflection, using white light.

The flow is remarkably stable when the inner disk and the outer ring are concentric. However, when the disk and the ring are no longer concentric, each image exhibits a chaotic aspect; the film thickness no longer arranges itself in an orderly fashion but a large vortex forms in the large gap region between the disk and the ring, as is illustrated in figure 29(b). The thickness starts to fluctuate in both space and time in the vortical region formed between the disk and the ring, as seen in figure 30. This magnified image is centred on the counter-rotating vortex that the off-centre disk generates.

An understanding of the statistics of this mixing can reveal valuable information on the interplay between the thickness and the velocity field in these rapidly moving soap films. The power spectrum of the thickness fluctuations was deduced from 2D Fourier transforms of images of small regions of the film in the chaotic region. A monochromatic light source was used.

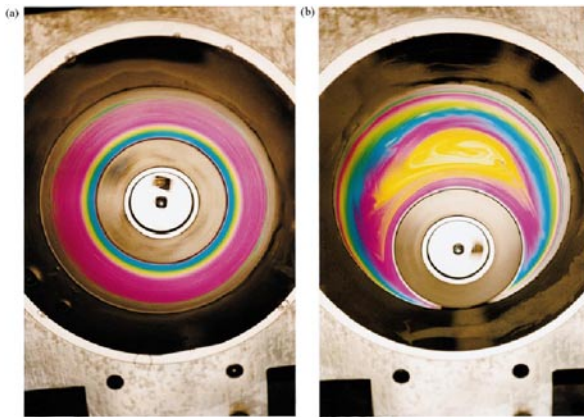


**Figure 29.** Flow patterns for a concentric (a) and an eccentric (b) set-up. The pictures are taken with a white, broad light source. The colour seen in the picture is due to the interference of light of different wavelengths. The film spans the annular region between a rapidly rotating inner disk and a fixed outer ring. The diameters of the disk and the ring are 5 and 10 cm, respectively. The rotation speed is approximately 20 Hz, which corresponds to a linear velocity of  $3 \text{ m s}^{-1}$  at the edge of the disk. The texture seen in the film (b) resembles that of chaotic advection of dye in a fluid.

(This figure is in colour only in the electronic version)

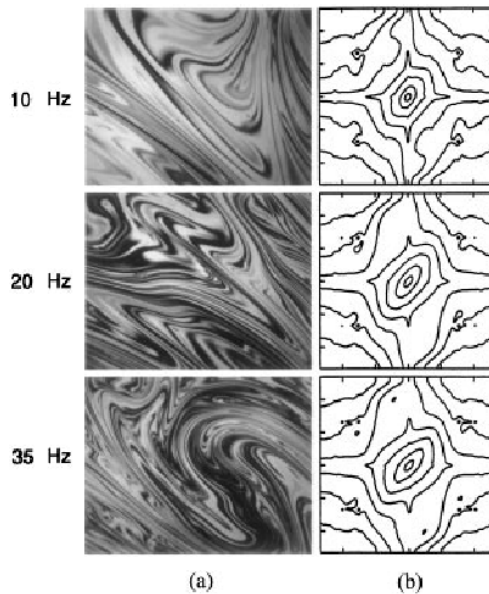


**Figure 30.** Flow patterns in an eccentric Couette cell. The pictures (a) are taken at the driving frequencies  $\Omega/2\pi = 10$  (upper), 20 (middle) and 35 Hz (lower), corresponding to  $Re = 4000$ , 8000 and 14 000, respectively. The size of the pictures is a small area,  $1 \times 1 \text{ cm}^2$ , in the centre of the large vortex. The right column (b) shows the corresponding time averaged power spectra,  $\ln[S(k_x, k_y)]$ , at  $\Omega/2\pi = 10$ , 20 and 35 Hz. Displayed are contours of constant  $S$ . The long axis of the ellipse in the centre of the graph corresponds to the  $k_y$  direction. The sharp peaks at  $45^\circ$  to the axes and the cusps along the axes in the contour plots are an experimental artefact due to finite pixel size; they contribute to  $S(k_x, k_y)$  only for  $k > 20 \text{ cm}^{-1}$ .

Wu *et al* show that, when the thickness fluctuations  $\delta h(x, y, t) = h(x, y, t) - h_0$  are small with respect to the mean thickness  $h_0$ , one can relate the reflected intensity to the fluctuating thickness directly. They also argue that  $\delta h(x, y, t)$  behaves as a passive scalar. This passivity implies that the thickness variations do not react back on the flow field and modify it. The 2D thickness spectra can be compared directly to theories concerning the mixing of a passive scalar in a chaotic flow field. However, one must check that the thickness is acting as a passive scalar first, i.e. that fluctuations in thickness do not react back on the velocity field. To analyse the experimental results, Wu *et al* make use of the equations of motion of the film coupled to the thickness as previously done by Couder and coworkers [20, 21]. They add another term in the equation for  $h(x, y, t)$  which takes into account the flow of interstitial water relative to the surfaces of the film [23, 33]:

$$\frac{\partial h}{\partial t} + \mathbf{v} \cdot \nabla h = -\kappa \nabla^4 h - h_0 \nabla \cdot \mathbf{v}. \quad (25)$$

Here  $\mathbf{v}$  is the 2D velocity of the film,  $h$  is the fluctuating thickness of the film,  $\nabla$  is the 2D divergence and  $\kappa$  plays the role of a diffusivity. The appearance of the  $\nabla^4 h$  term is related to the fact that the flow of fluid in the film is assumed to obey Darcy's law. The last term in the right-hand side of (25) takes into account the compressibility of the film, since  $h$  can fluctuate. This term turns out to be small compared to the convective term and will therefore be ignored.

Equation (25) must be supplemented by the velocity equation which can be written as

$$\frac{\partial \mathbf{v}}{\partial t} + \mathbf{v} \cdot \nabla \mathbf{v} = -\frac{C^2}{h_0} \nabla h + \nu \nabla^2 \mathbf{v}. \quad (26)$$

Here  $\nu$  has its previous meaning,  $C = \sqrt{E/\rho h_0}$  is the speed of elastic waves in the soap film,  $E$  is the elasticity of the film and  $\rho$  is the density of water. The term proportional to the gradient of  $h$  in (26) takes into account the variations of the local pressure due to the fluctuations of the interfaces.

Equation (25) resembles the diffusion equation for a passive dye except for the presence of the fourth derivative term due to a different relaxation process for the thickness and for the nonzero divergence of the velocity field. Since large-scale shear dominates in this experiment, the second term on the right-hand side of (25) can be neglected with respect to the convective term on the left-hand side of the equation.

In order to go further, it is shown that the nonlinear terms in the Navier–Stokes equations are large compared to the reaction of elastic forces in the soap film. The flow field stretches or compresses the film which reacts elastically; this elastic response is estimated to be small compared to the velocity, permitting the conclusion that the elasticity of the film does not modify the flow significantly. The above equation for  $h$  then becomes equivalent to the equation for a passive scalar  $\Phi$ —if the film is driven sufficiently hard that the nonlinear term (inertial term) of the Navier–Stokes equation is larger than the thickness contribution. The authors note that the observed mixing resembles closely the patterns observed in the mixing of a dye in a chaotic flow [34].

The measurements and analysis presented above motivate a comparison with a theory by Batchelor [35] concerning the mixing of a dye or of temperature fluctuations in the viscous diffusive range of a turbulent flow. The viscous–diffusive subrange is located at sufficiently small scales that no eddies are present and velocity fluctuations are strongly damped but strong enough to produce stretching and folding of the dye concentration field, say, or temperature field.

Batchelor's theory predicts a density spectrum of the dye or temperature fluctuations to scale as  $E_h(k) \simeq k^{-1}$ . Typical power spectra of the thickness fluctuations  $S(k)$  are shown in figure 30, along with the thickness field in a small region within the vortical region of the flow.

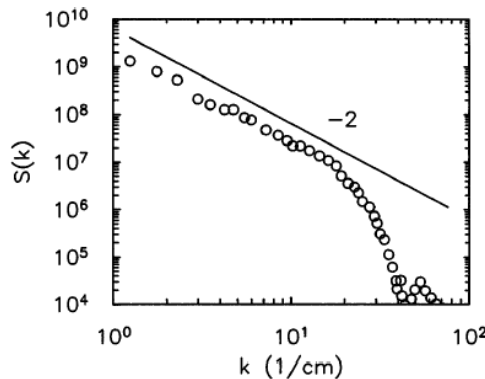


**Figure 31.** Scaling form of the spectral density  $S_h(k)$  along  $\theta = 45^\circ$ . The full line with a slope of  $-2$  is a guide to the eye. The Reynolds number is 8000.

The spectra are not isotropic because the randomization of the fluctuations is not complete even for the larger rotation frequencies used.

The spectrum along a cut at  $45^\circ$  is shown in figure 31. Note that over roughly a decade in  $k$  the thickness power spectrum, labelled here as  $S_h(k)$ , shows a scaling range with an exponent of  $-2$  which corresponds, in 2D, to

$$E_h(k) = k S_h(k) \propto k^{-1},$$

as expected from Batchelor's theory. Cuts along other directions give similar spectra with a similar exponent. The success of this comparison strongly suggests that thickness fluctuations in rapidly flowing soap films indeed act as a passive scalar. These fluctuations can therefore provide valuable information about the statistics of mildly turbulent flows of the type generated in this experiment—and perhaps in strongly turbulent flows as well.

#### 4.3. Work on thin fluid layers on solid substrates

**4.3.1. Decay of 2D turbulence using an electrolyte fluid layer driven magnetically.** This study focuses mainly on the properties of decay of an initially organized array of vortices [36]. The system studied is a thin layer of conducting fluid (an electrolyte) driven magnetically by an array of magnets and electrically with a constant current traversing the layer. The set-up is shown in figure 32. The cell is made of PVC with a thin glass plate as the bottom layer. A square array of permanent magnets (with a vertical magnetization axis and a magnetic field of about 0.3 T) with alternating poles is placed below the cell.

The fluid is a mixture of sulfuric acid in water and hence is strongly conducting. The depth of the fluid layer is typically a few millimetres. A well regulated current source is used to inject an electric current into the solution from one side of the cell to the other with a typical value of 300 mA. Visualization of the flow is accomplished by adding small neutrally buoyant particles which float on the surface of the solution and follow the flow field.

Particles are tracked with a CCD camera and homemade software. A time series of the data enable determination of the evolution of the velocity, the stream function and the vorticity. The experiments are carried out by first imposing a current to drive the flow. The initial flow is an organized array of alternating vortices as seen in figure 33. The current is switched off and the array of vortices decays to an equilibrium state through several vortex merging events.

Figure 34 shows a photograph of the flow one second after current injection is switched off. Note that the initial regular array of vortices becomes disorganized. The figure displays

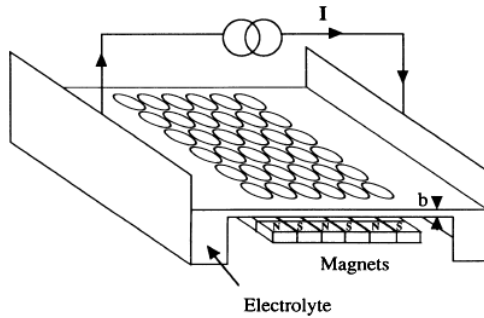


**Figure 32.** Schematic representation of the experimental system (not to scale); the walls confining the flow and the lateral limits of the cell are not represented.

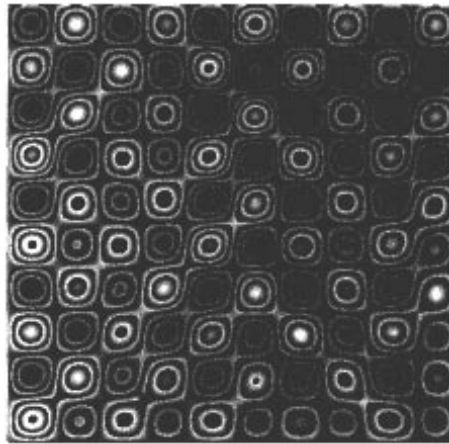


**Figure 33.** Vorticity at  $t = 0$  for the same conditions as in figure 2.

the velocity field, stream function and vorticity field. By following the decay phase through measurements of the velocity of trace particles on the surface, Cardoso *et al* [36] arrive at the evolution of different physical quantities such as total energy, enstrophy, vortex size, vortex separation and vortex density as time elapses. The results are then compared to different theories concerning the decay of 2D turbulence.

While the measurement of the energy and of the enstrophy is straightforward, the determination of vortex size, separation and density is not. The authors define these quantities as:  $E = \int u^2 dS$ ,  $Z = \int \omega^2 dS$  and  $a(t) = \sqrt{E/Z}$ , where  $u$  is the velocity vector,  $\omega$  is the vorticity,  $E$  is the total energy,  $Z$  is the enstrophy and  $a$  is the vortex size. The vortex density and separation are evaluated differently: the authors calculate the extrema of the stream function which correspond to the position of the vortices. From localizing and counting these extrema the authors deduce a vortex density  $\rho(t)$  and vortex mean separation  $r(t)$ .

Typical results for the decay of energy and enstrophy are shown in figure 35. Note that both the energy and the enstrophy decay exponentially after the cessation of current injection. However, the enstrophy seems to decay faster than the energy in the initial period of decay. The exponential decay of the energy is attributed to viscous effects due to the bottom substrate. The initial fast decay of the enstrophy is attributed to the presence of numerous merging events during this period.

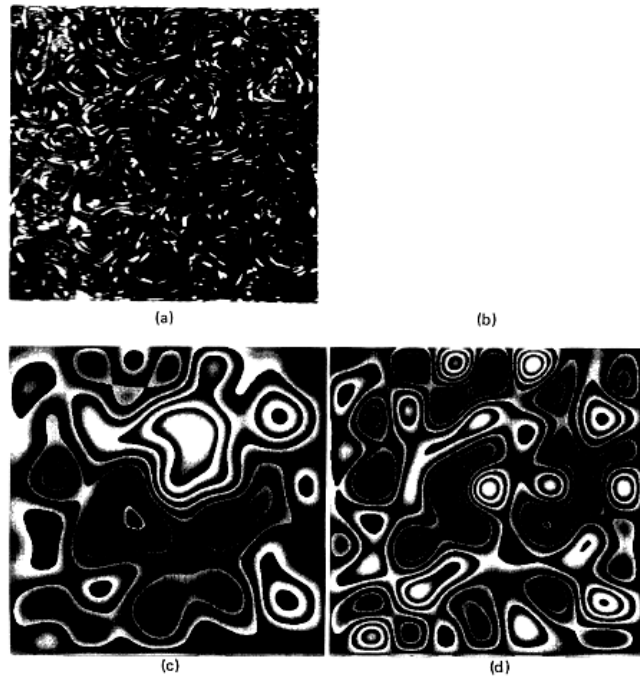


**Figure 34.** Freely decaying turbulence from an ordered lattice of 100 vortices obtained at  $I = 300$  mA for 1.2 s, with a thickness  $b = 3$  mm. An image of the flow is taken 1 s after the sudden quench of the electric current. The size of the system ( $80 \times 80$  mm $^2$ ) gives the scale of the figures: (a) direct image of the flow average over 10 frames ( $\frac{1}{3}$  s); (b) corresponding velocity field computed using correlation zone of size  $\lambda = 32$  and a time interval  $\partial t = 0.04$  s; (c) computed stream function based on the velocity field (b); (d) computed vorticity field based on the velocity field (b).

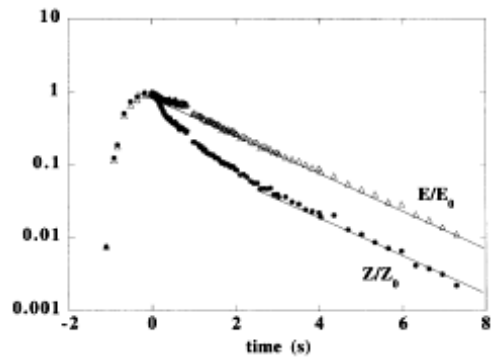


**Figure 35.** Decay of the energy and the enstrophy for a system of 100 vortices, with  $b = 3$  mm, an initial value of  $I$  of 400 mA, and  $t = 100$  ms (the ordinates have been renormalized to 1 for  $t = 0$ ).

The geometrical properties of the decay and their temporal evolution is shown in figure 36. The density, mean separation between vortices and the vortex size all display scaling behaviour as time elapses. The results show that the density of vortices decreases in time while the mean separation and the vortex size increase as time increases, in agreement with the visual observation of several merging events. The results can be approximated by the following

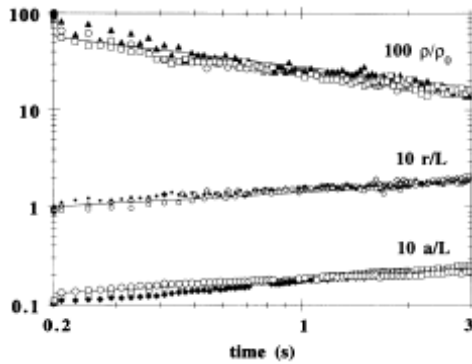


**Figure 36.** Temporal evolution of the vortex densities  $\rho/\rho_0$  (where  $\rho_0$  is the value for  $t = 0$ ), the mean distance between vortices  $r(t)/L$  and the mean vortex sizes  $a(t)/l$  (where  $L$  is the system size) for systems of 100 vortices,  $b = 3$  mm, and several initial values of the energy, corresponding to values of the Reynolds number  $\sqrt{E}L/v$  of the order of 1000.

relations:  $\rho(t) \sim t^{-0.44}$ ,  $a(t) \approx r(t) \sim t^{0.22}$ . These are to be compared to Batchelor's predictions which state that the vortex size and mean separation should increase linearly with time while the density should decrease as the square of the time. Clearly the experimental values for the exponents are very different from these theoretical predictions.

An interesting observation in this experiment is that the system stays dense with vortices, i.e. they occupy the whole space available during the decay phase. Indeed, the density of the vortices multiplied by the square of the mean size  $\rho a^2$  stays roughly constant during the whole decay phase. While this is in agreement with Batchelor's theory, which also predicts that the system stays dense, large discrepancies are found for the evolution of the separate parameters characterizing the system.

There are other theories in the literature about this decay phase, but again the experiments do not agree with these either. One of these theories supposes that, instead of an invariant energy, it is the maximum vorticity which is invariant [37]. The experimental results do not show this behaviour as the maximum vorticity is found to decrease as the square root of the enstrophy. The problem of decaying turbulence is thus far from resolved. While the present experiments indicate deviations from expected laws, the soap film experiments of Couder [3] and Martin *et al* [31] do show agreement with Batchelor's predictions.

**4.3.2. Forced turbulence.** Paret and Tabeling [39, 41] have also used a different drive in their magnetically driven fluid layers to obtain a sustained turbulent flow. The system is now driven by an ac current source, namely a series of pulses of alternating sign. The fluid was stratified in density to minimize friction against the bottom surface of the container. The upper fluid layer is driven by the flow beneath it, because the range of the magnetic field does not extend above the bottom layer. Supposedly this scheme avoids a good part of the friction due to the solid surface. This new driving scheme gave rise to a turbulent flow and an inverse energy cascade scaling for about half a decade in wavenumbers. Using this same scheme, but now with forcing at larger scales, the data display an enstrophy cascade interval as well.

Figure 37 shows the energy density spectrum obtained for a forcing at small scales and showing for about half a decade a scaling range consistent with the  $-5/3$  scaling expected for forced turbulence in 2D. The figure also shows the temporal evolution of the spectrum from its initial state to its final stationary state. Initially, a bump is observed at the scale of injection, then, progressively, the spectrum builds up to show a range of inverse cascade scaling.

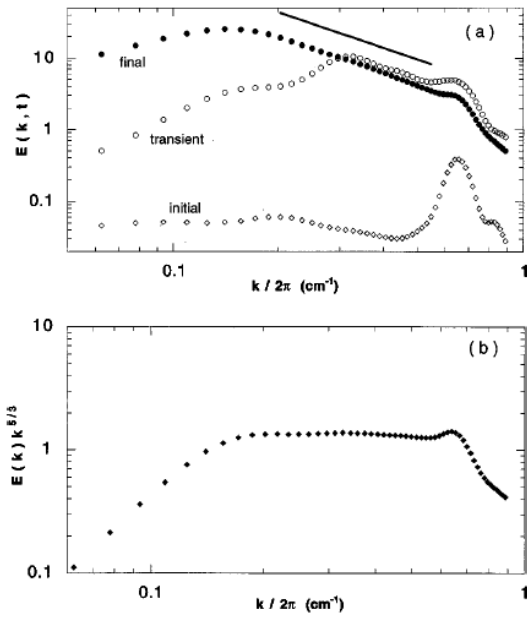


**Figure 37.** Energy spectra. (a) Temporal evolution; (b) compensated energy spectrum for the stationary regime.

Paret and Tabeling also determine the Kolmogorov constant  $C$  as discussed earlier in the experiment of Sommeria and find a value of 6.5. In addition to the determination of the spectral properties of the turbulent velocity field, the authors [41] also presented a study of the structure functions of the velocity as well as their probability density functions. The results showed that the PDFs have a Gaussian shape for all the scales probed in this range.

There now exists a number of numerical studies of forced 2D turbulence that offer convincing evidence that deviations of  $P(\delta v(r))$  from Gaussianity are measurable but small [42]. Of course,  $P$  cannot be purely Gaussian, since the third moment in the forced case must be positive and proportional to  $r$  in the inverse cascade range.

In the experiments of Paret and Tabeling, the structure functions were analysed using the so-called extended self-similarity (ESS) method. In fact the structure functions plotted directly against the scale  $r$  did not display a good scaling (figure 38(a)); however, when the authors examined the variation of the structure functions versus the third-order structure function, which is the implementation of the ESS method, they extracted exponents that showed ‘normal’ behaviour. This means that  $S_n(r) \sim (S_3(r))^{n/3}$  which is shown in figure 38(b). The authors conclude that the inverse cascade shows no ‘intermittency’ in contrast to the case of fully developed 3D turbulence.

Using a variant of this set-up to ensure forcing at much larger scales, Paret *et al* [40] also present evidence for an enstrophy cascade range with a scaling exponent close to the expected value,  $b = 3$ , in equation (24). To accomplish this, the magnets were arranged in four triangular clusters, with the magnetic orientation being similar in each cluster. The authors argue that this arrangement should not favour any permanent pattern. The driving current is still a series of square pulses with alternating signs but is not periodic as in the previous realization.

The energy density spectrum displayed in figure 39 is in good agreement with the expected behaviour based on the phenomenological theory of Kraichnan. The structure functions of the

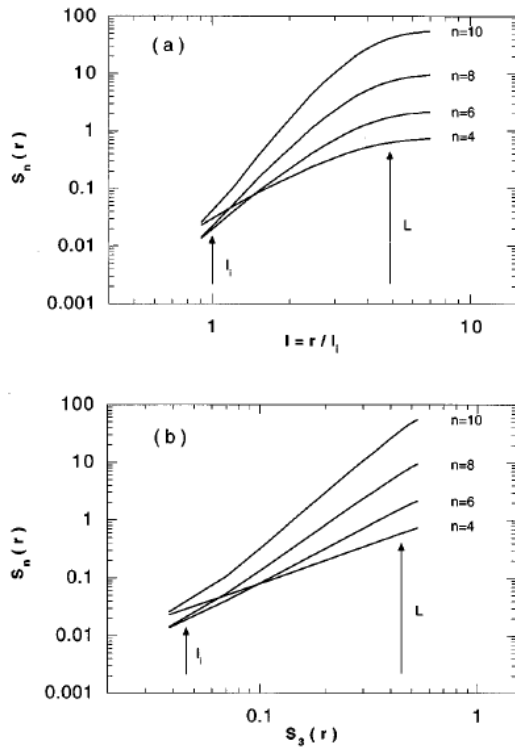


**Figure 38.** Longitudinal velocity structure functions  $S_u^{\parallel}(r)$  as a function of (a) the nondimensional scale  $l = r/l_t$  and (b)  $S_3^{\parallel}(r)$  for  $n = 4, 6, 8$  and 10. The injection scale  $l_t$  and the integral scale  $L$  are indicated.

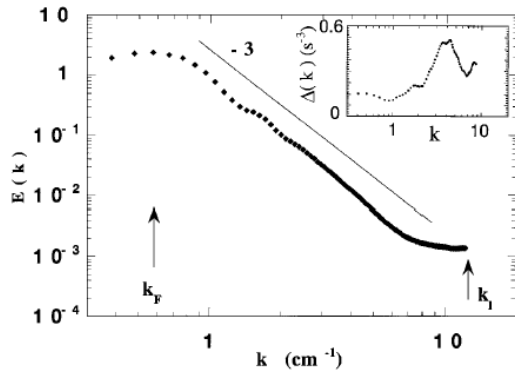


**Figure 39.** Energy spectrum of the velocity field, averaged over 200 realizations of the velocity field in the statistically stationary state; the inset shows the enstrophy transfer rate  $\Delta(k)$ , calculated in similar experimental conditions.

vorticity increments showed little variation with the scale  $r$  for a range of scales ranging from 1.5 to 7 cm (the box had dimensions of  $15 \times 15$  cm) as shown in figure 40. This is also as expected in the enstrophy range.

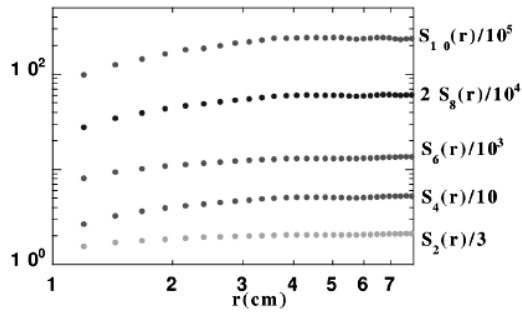


**Figure 40.** Structure functions of the vorticity increments for various orders comprised between 2 and 10.

#### 4.4. Mixing of a passive scalar

Amongst the few firm results in the theory of turbulence is Batchelor's prediction about the form of the spectrum  $E_\theta(k)$  of a passive scalar in the convective-dissipative range of wavenumbers. A soap film experiment, discussed above [23], is in accord with the prediction,  $E_\theta(k) \propto k^{-1}$ , in this range. However, the quantity measured in that work was the thickness  $h(x, t)$ ; it is not truly a passive scalar, though in certain limits it is expected to act like one. The experiment now to be described was aimed at testing the Batchelor prediction, using a fluorescent dye, which is a passive scalar beyond any doubt.

The experiment was carried out by Williams *et al* [49]. The set-up was similar to that of Paret and Tabeling [39]. The working fluid in the experiment consists of two layers of fluid: a solution of water and salt as the bottom layer (3 mm thick) and fresh water for the upper layer (about 1 mm thick). As the upper layer is not conductive, the driving of this layer is due to the movement of the bottom layer. The array of magnets used had two different configurations: either spatially periodic or random. The current used is also either constant or time-periodic as a series of pulses.

In order to study mixing, a fluorescent dye was added to fresh water which was then injected into the upper layer. Excess solution was then removed at the same rate to ensure a stationary state for the dye concentration. Images of the dye fluorescence were then digitally recorded and then Fourier analysed to obtain the spatial power spectrum of the passive dye concentration. The experiment was intended to be an explicit test of the Batchelor prediction for the mixing of a passive dye in the range of scales where the turbulence is in its dissipative range. In this range the flow should be composed of a random straining of fluid elements.

Williams *et al* measure both the velocity field and the dye concentration field. A measurement of the velocity fluctuations is crucial if the test is to be conclusive to ensure that the explored scales lie in the viscous-convective range. This range is bounded at small and large wavenumbers by  $k \simeq \epsilon^{1/4} v^{-3/4}$  (where the scale-dependent Reynolds number is unity) and  $k \simeq \sqrt{\gamma/\kappa}$ , where  $\kappa$  is the diffusivity of the scalar and  $\gamma$  is the average strain rate.

From velocity measurements, Williams *et al* determine that this range lies at scales below 1 cm; they also estimate that this range should extend down to about 0.014 cm. A typical snapshot of the dye concentration field is reported in figure 41. The scalar spectra are shown in figure 42. As can be noted here, the spectra are generally steeper than the  $k^{-1}$  dependence expected from Batchelor's theory. The arrow in the graph indicates the range of scales where the viscous-convective range is expected. Actually, the data above  $20 \text{ cm}^{-1}$  should not be taken into account, as this is basically the noise floor.

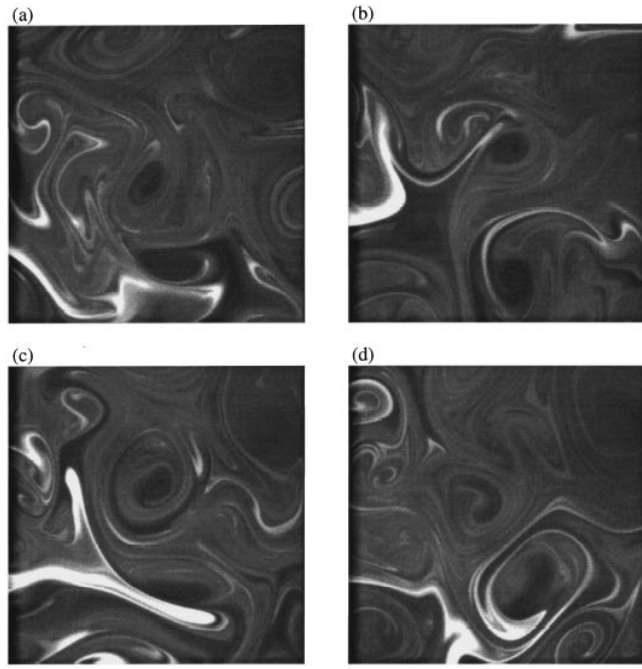


**Figure 41.** Sample images of the concentration field during mixing, for the random magnet array of figure 2(b). A  $10.2 \times 10.2$  cm region is shown at 5 s intervals.

Over the whole range studied here, no convincing  $k^{-1}$  range is observed. Different situations were tested in this experiment, such as a random and periodic array of magnets as well as a more viscous fluid (a mixture of water and glycerol) to minimize the effects of vertical velocity gradients.

No convincing evidence of the Batchelor scaling was found. A possible source of the discrepancy between theory and experiment is the presence of the large coherent structures in this flow; the authors argue that their presence renders the flow highly intermittent and ask the question if such an intermittent situation still allows such scaling for the dye concentration. Clearly more experiments are needed to establish the existence or nonexistence of the Batchelor scaling for the viscous convective range in two dimensions.

More recently Jullien *et al* [52] studied the dispersion of a fluorescent dye in the enstrophy cascade range of scales in a set-up similar to the one of Paret *et al* [40]. This work differs from the study of Williams *et al* [49] in that the velocity field shows an enstrophy cascade and the dissipative range for this field is at smaller scales than the ones studied. The dye was injected as a blob at a scale close to the scale of injection of the energy. A scaling of the scalar spectrum was observed for a little over half a decade for scales smaller than the injection scale. The scaling exponent is consistent with  $-1$  as would be expected in the enstrophy range of scales [14]. The structure functions showed variations consistent with a logarithmic increase while the probability density functions of the scalar increments exhibit exponential tails. Both these findings are consistent with theoretical expectations for a scalar field in two dimensions driven by a large-scale random strain [54]. The photographs in figure 43 show the evolution of the dye pattern at different times after the injection. Figure 44 shows the power spectrum of the scalar concentration fluctuations to illustrate the scaling law observed.

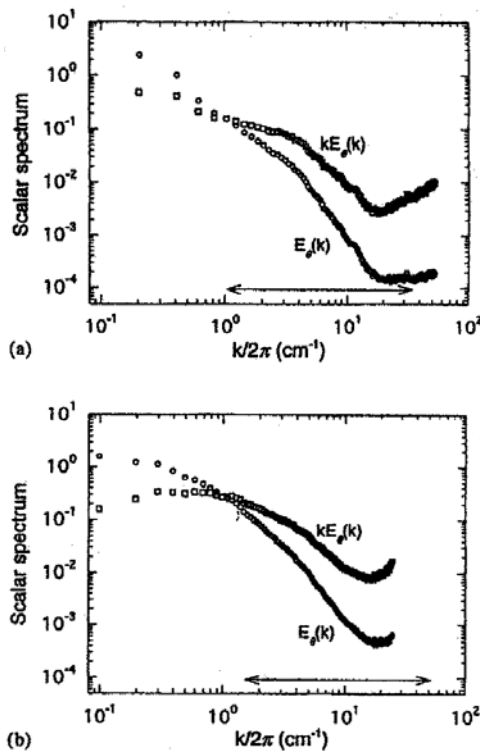


**Figure 42.** One-dimensional concentration spectra (normalized by the variance) for two magnet arrangements: (a) regular and (b) random. Also displayed are the compensated spectra  $kE_0(k)$  that would appear flat for  $k^{-1}$  scaling. The estimated viscous-conductive range is indicated by an arrow. The structure for wavenumbers greater than  $k/2\pi = 15 \text{ cm}^{-1}$  in (a) and  $k/2\pi = 10 \text{ cm}^{-1}$  in (b) is obscured by noise.

In an even more recent study, Jullien *et al* [53] also examined the tracer dispersion in the inverse energy cascade range. Here the expected scaling of  $-5/3$  for the scalar density spectrum was observed.

## 5. Relative dispersion

Relative diffusion in the atmosphere has been investigated since the early work of Richardson and represents one of the fundamental aspects of turbulence. In this paper Morel and Larcheveque (M&L) use a large set of balloon pairs to determine their relative separation as a function of time and initial separation [15]. They focus mostly on medium and large scales to test whether the atmospheric turbulence at these scales possesses 2D aspects. Some previous observations and theoretical arguments show that this could be the case.

Theoretically, the problem of relative diffusion in two dimensions and its relation to atmospheric turbulence at large scales was treated by Lin [16], who showed that the relative separation of two particles following the flow increases exponentially with time in the enstrophy range, where the diffusivity varies as the square of the initial separation.

The M&L experiment uses 483 constant-volume balloons at the 200 mb level in the southern hemisphere. The positions of the balloons were followed by satellite (EOLE data collection and navigation satellite). The data was collected during the period October 1971 to

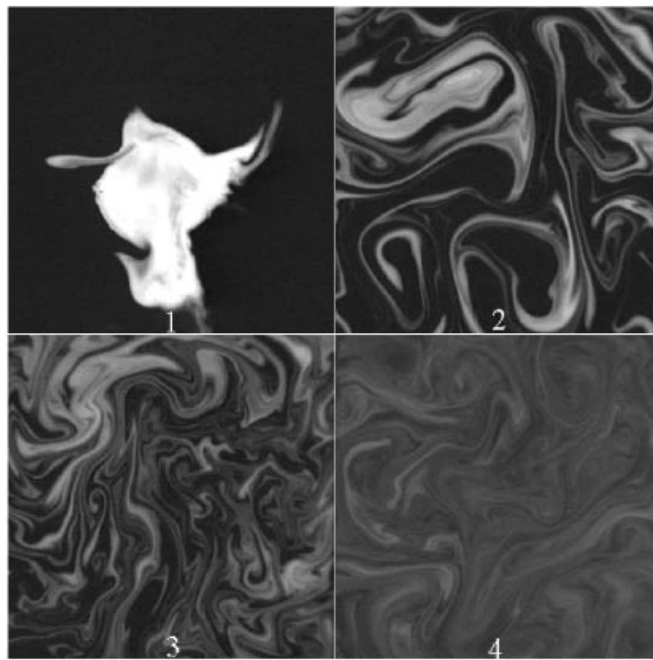


**Figure 43.** Time evolution of a blob of fluorescein of density  $\rho = 1002 \text{ g l}^{-1}$  in a  $16 \text{ cm} \times 16 \text{ cm}$  region, at times  $t = 1, 12, 20$  and  $40 \text{ s}$ .

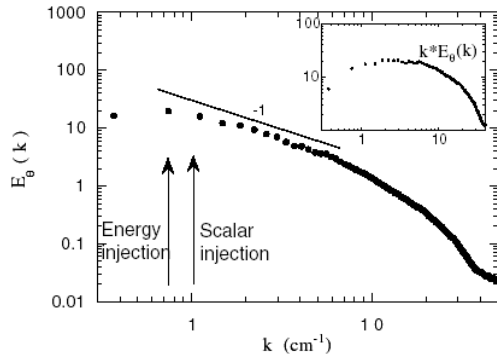


**Figure 44.** Variance scalar spectra with a pollutant of density  $\rho = 1002 \text{ g l}^{-1}$ ; the straight line has a  $k^{-1}$  slope. The inset shows the compensated spectra  $E_\theta(k) \times k$ .

January 1972. The set of data consisted of twelve thousand individual measurements of the relative dispersion rate of the balloon pairs. The dispersion rate of the pair was calculated as

$$dD^2/dt = (D^2(t_2) - D^2(t_1))/(t_2 - t_1)$$

where  $D(t)$  is the separation distance between two balloons at time  $t$  (the separation  $D$  was called  $r$  in the theoretical section). These distances were split into a group of 14 sets of separations between 0 and 60 km for the first set and into separations between 4000 and 10 000 km for the last set.

Before proceeding to extract the diffusivity and the dispersion law, M&L check for homogeneity, stationarity and isotropy of the flow. Their length scales span the range 10–

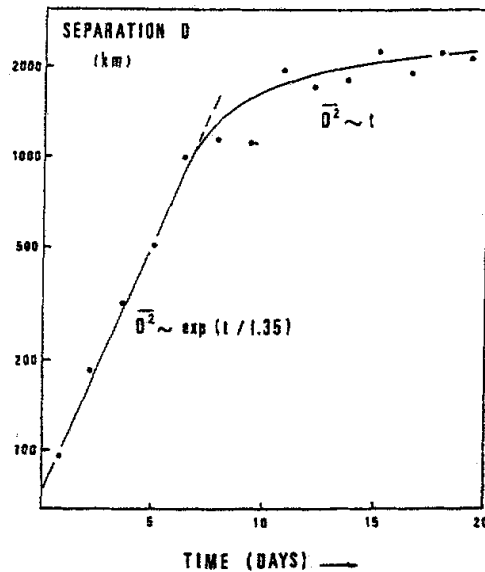


**Figure 45.** Root mean square separation of the original pairs of balloons released during the EOLE experiment as a function of time after launch.

10 000 km. They find that the diffusivity is homogeneous and stationary since data was reproducible from different realizations taken at different positions and at different times. Further, the diffusivity is found to be isotropic for the range of scales between 100 and 1000 km, as the diffusivity was similar in both zonal and meridional directions. This is no longer true for separations exceeding 1500 km.

As noted above, the theory of Lin (and a simple dimensional argument) predicts an exponential growth law for the mean square particle separation as a function of time in the enstrophy range. The authors test this prediction directly with their measurement. This exponential growth is apparent in figure 45, which depicts the variation of the mean square distance between balloon pairs as a function of time. The striking agreement between the experimental results at early time with the prediction of Lin shows that, for the scales covered, atmospheric turbulence may be characterized by the idea of an enstrophy cascade. A further test of this conclusion is provided by a measurement of the relative diffusion rate as a function of separation  $D$ . Figure 46 shows the results of the diffusivity as a function of distance on a log-log plot. According to the theory of Lin, one expects a variation of  $d\bar{D}^2/dt$  as  $\bar{D}^2$  in the enstrophy range. The measurements of M&L indeed show this expected dependence. Again, for scales between 100 and 1000 km, good agreement is found with the expectations of the theory based on a cascade of enstrophy in 2D turbulence. Observe that the variation of the diffusivity versus separation  $D$  is directly related to the scaling of the energy density spectrum.

Relative diffusion has also been studied experimentally in a magnetically driven fluid layer, using the apparatus described in [39]. In this experiment by Jullien *et al* [50], polystyrene latex particles with a diameter of  $2 \mu\text{m}$  are placed in clusters, which subsequently diffuse under the action of the underlying turbulence. The quantity measured is the mean square separation,  $\sigma^2(t)$  (noted  $\bar{D}^2$  above), of  $10^4$  particle pairs. Jullien *et al* find that over a decade to time,  $\sigma^2(t)$  varies as  $\sigma^2(t) \propto t^3$  as seen in figure 47. Figure 48 shows typical trajectories of a pair

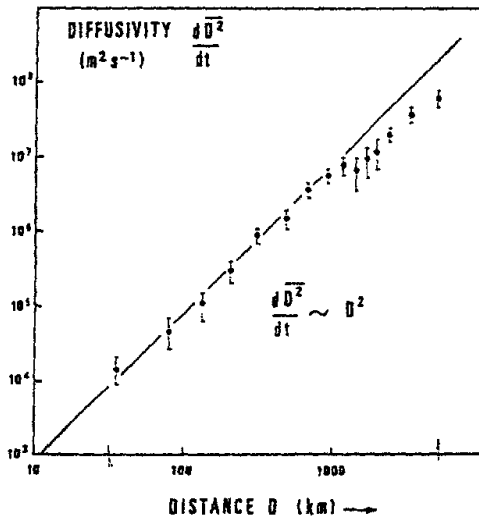


**Figure 46.** As in figure 45 except for mean diffusivity. The  $D^2$  law (full line) also corresponds to the  $k^{-2}$  energy spectrum.

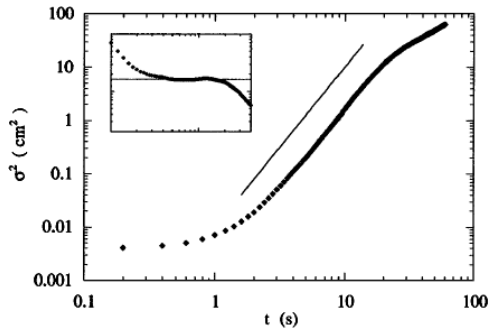


**Figure 47.** Time evolution of the mean square separation of  $10^4$  pairs of particles. Inset: the same curve divided by  $t^3$  showing the existence of the Richardson regime.

of particles released close to each other and followed in time. This is the behaviour expected from Richardson–Kolmogorov argument in the energy cascade range.

In the enstrophy range, where the enstrophy injection rate  $\beta$  is presumably controlling, the same reasoning leads to an exponential growth of  $\sigma^2(t)$ , which was seen by Morel and Larcheveque in the experiment discussed above: repeating this dimensional argument,  $d\sigma^2(t)/dt \propto \beta^{1/3}\sigma^2$ , which implies that  $\sigma^2(t) = \sigma^2(0)e^{\beta^{1/3}t}$ .

The results of [50] are somewhat surprising, since the initial separation of the particles is sufficiently small that one might suspect that, for small  $t$ , the measurements would be within the enstrophy cascade range, or possibly the dissipative range, where the above dimensional argument should also apply.

One possible resolution of this puzzle is that the surface particles, while moving in 2D, can exchange energy and enstrophy with the underlying thin layer of fluid below. Recent experiments [51] show that particles floating on a deep and turbulent body of water exhibit 3D-like behaviour.

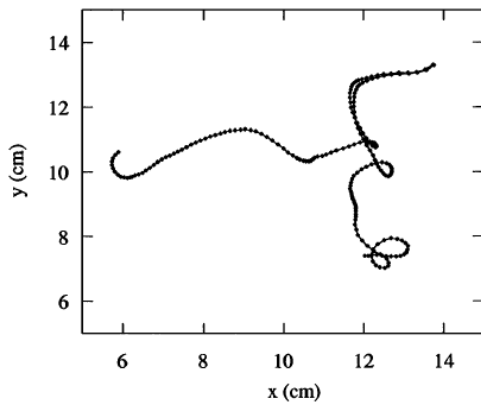


**Figure 48.** Typical trajectories for a pair of particles, released at the upper right of the figure, with an initial separation of 0.03 cm; the time interval between two successive dots is 0.2 s.

## 6. Conclusion

In this review we have discussed a range of experiments concerning almost 2D turbulence in a 3D world. The present body of work supplies convincing evidence from two different experimental systems of both a direct cascade of enstrophy at small scales and an inverse cascade of energy at scales larger than the scale on which turbulence is generated. The experiments reveal that in 2D forced and decaying turbulence are very different. No such distinction appears to exist in 3D. Recent work has also focused on a finer study of structure functions and probability density functions of velocity and vorticity increments. These experiments, which yield valuable information about the statistical laws governing turbulence, should lead to a better assessment of theory. Progress has also been made in the passive scalar problem where some theoretical ideas and scaling laws have been tested.

## References

- [1] Sommeria J 1986 *J. Fluid Mech.* **170** 139 (reference 31)
- [2] Couder Y 1981 The observation of a shear flow instability in a rotating system with a soap membrane *J. Physique Lett.* **42** 429
- [3] Couder Y 1984 Two-dimensional grid turbulence in a thin liquid film *J. Physique Lett.* **45** 353
- [4] Fine K S *et al* 1994 Relaxation of 2D turbulence to a metaequilibrium near the minimum enstrophy state *Phys. Rev. Lett.* **72** 2187
- [5] Frisch U 1995 *Turbulence* (Cambridge: Cambridge University Press)
- [6] Kolmogorov A N 1941 The local structure of turbulence in an incompressible fluid for very large Reynolds numbers *Dokl. Akad. Nauk* **30** 301 (*Proc. R. Soc. A* **434** (reprinted))
- [7] Landau L D and Lifshitz E M 1993 *Fluid Mechanics* 2nd edn (New York: Pergamon)
- [8] Richardson L F 1926 Atmospheric diffusion shown on a distance-neighbor graph *Proc. R. Soc. A* **110** 709
- [9] Belmonte A, Goldburg W I, Kellay H, Rutgers M A, Martin B and Wu X L 1999 Velocity fluctuations in a turbulent soap film: the third moment in two-dimensions *Phys. Fluids* **11** 1196
- [10] Kraichnan R 1967 Inertial ranges in two-dimensional turbulence *Phys. Fluids* **10** 1417
- [11] Kraichnan R H and Montgomery D 1980 Two-dimensional turbulence *Rep. Prog. Phys.* **43** 547
- [12] Kraichnan R H 1971 Inertial-range transfer in two- and three-dimensional turbulence *J. Fluid Mech.* **47** 525
- [13] Falkovich G and Lebedev V 1994 Universal direct cascade in two-dimensional turbulence *Phys. Rev. E* **50** 3883
- [14] Lesieur M 1990 *Turbulence in Fluids* 2nd edn (Dordrecht: Kluwer)
- [15] Morel P and Larcheveque M 1974 Relative dispersion of constant-level balloons in 200 mb general circulation *J. Atmos. Sci.* **31** 2189

- [16] Lin J T 1972 Relative dispersion in the enstrophy cascade range of homogeneous two-dimensional turbulence *J. Atmos. Sci.* **29** 394
- [17] Batchelor G K 1969 Computation of the energy spectrum in homogeneous two-dimensional turbulence *Phys. Fluids (Suppl.)* **2** 233
- [18] Saffman P G 1971 *Stud. Appl. Math.* **50** 277
- [19] Eyink G 1995 *Phys. Rev. Lett.* **74** 3800
- [20] Couder Y, Chomaz J M and Rabaud M 1989 *Physica D* **37** 384–405
- [21] Chomaz J M and Cathala B 1990 *Phys. Rev. A* **41** 2243
- [22] Wu X L *et al* 2000 An infrared technique for measuring thickness of a flowing soap film *Preprint*
- [23] Wu X L, Martin B, Kellay H and Goldburg W I 1995 *Phys. Rev. Lett.* **75** 236
- [24] Mysels K J, Shinoda K and Frankel S 1959 *Soap Films Studies of Their Thinning* (New York: Pergamon)
- [25] Gharib M and Derango P 1989 *Physica D* **37** 406
- [26] Kellay H, Wu X L and Goldburg W I 1995 *Phys. Rev. Lett.* **74** 3975
- [27] Rutgers M A, Wu X L, Bhagavatula R, Petersen A A and Goldburg W I 1997 *Phys. Fluids* **8** 2847
- [28] Tong P, Goldburg W I, Chan C K and Sirivat A 1988 *Phys. Rev. A* **37** 2125
- [29] Rivera M, Belmonte A, Goldburg W I, Wu X L and Kellay H 1998 *Rev. Sci. Instrum.* **69** 3215
- [30] Chasnov J 1997 *Phys. Fluids* **9** 171
- [31] Martin B, Wu X L, Goldburg W I and Rutgers M A 1998 *Phys. Rev. Lett.* **80** 3964
- [32] Kellay H, Wu X L and Goldburg W I 1998 *Phys. Rev. Lett.* **80** 277
- [33] Bruinsma R 1995 Theory of hydrodynamic convection in soap films *Physica A* **216** 59
- [34] Ottino J M 1989 *The Kinematics of Mixing: Stretching, Chaos, and Transport* (New York: Cambridge University Press)
- [35] Batchelor G K 1958 *J. Fluid Mech.* **5** 8
- [36] Cardoso O, Marteau D and Tabeling P 1994 *Phys. Rev. E* **49** 454
- [37] Carnevale G F, McWilliams J C, Pomeau Y, Weiss J B and Young W R 1991 *Phys. Rev. Lett.* **66** 2735
- [38] Rutgers M A 1998 *Phys. Rev. Lett.* **81** 2244
- [39] Paret J and Tabeling P 1997 *Phys. Rev. Lett.* **79** 4162
- [40] Paret J, Jullien M C and Tabeling P 1999 *Phys. Rev. Lett.* **83** 3418
- [41] Paret J and Tabeling P 1998 *Phys. Fluids* **10** 3126
- [42] The latest study is Boffetta G, Celani A and Vergassola M 2000 Inverse energy cascade in two-dimensional turbulence: deviations from Gaussian behavior *Phys. Rev. E* **61** R29
- [43] Rivera M, Vorobieff P and Ecke R 1998 *Phys. Rev. Lett.* **81** 1417
- [44] Brachet M E, Meneguzzi M and Sulem P L 1986 *Phys. Rev. Lett.* **57** 683
- [45] Belmonte A, Martin B and Goldburg W I 2000 *Phys. Fluids* **12** 835
- [46] Rivera M and Wu X L 2000 *Phys. Rev. Lett.* **85** 976
- [47] Kellay H, Bruneau C H and Wu X L 2000 Probability density functions of the enstrophy flux in two dimensional grid turbulence *Phys. Rev. Lett.* **84** 1696
- [48] Vorobieff P, Rivera M and Ecke R E Soap film flows: statistics of 2D turbulence *Phys. Fluids* **11** 2167
- [49] Williams B S, Marteau D and Gollub J P 1997 Mixing of a passive scalar in magnetically forced two dimensional turbulence *Phys. Fluids* **9** 2061
- [50] Jullien M-C, Paret J and Tabeling P 1999 Richardson pair dispersion in two-dimensional turbulence *Phys. Rev. Lett.* **82** 2872
- [51] Goldburg W I *et al* Turbulence in a free surface *Phys. Rev. E* **63** 065303
- [52] Jullien M C, Castiglione P and Tabeling P 2001 *Phys. Rev. Lett.* **85** 3636
- [53] Jullien M V, Castiglione P and Tabeling P 2001 *Phys. Rev. E* **64** 035301
- [54] Chertkov M, Falkovich G, Kolokolov I and Lebedev V 1995 *Phys. Rev. E* **51** 5609  
Falkovich G, Kolokolov I, Lebedev V and Migdal A 1996 *Phys. Rev. E* **54** 4896  
Balkovsky E and Foucaux A 1999 *Phys. Rev. E* **60** 4164
- [55] Vorobieff P and Ecke R E 1999 *Phys. Rev. E* **60** 2953